Recovering *P–T–t* paths from ultra-high temperature (UHT) felsic orthogneiss: an example from the Southern Brasília Orogen, Brazil

Rafael G. Motta [a b c]

rafagmotta@gmail.com

Ian C. W. Fitzsimons [b]

i.fitzsimons@curtin.edu.au

Renato Moraes [c]

rmoraes@usp.br

Tim E. Johnson [b]

tim.johnson@curtin.edu.au

Sheila Schuindt [d]

s.schuindt.carmo@gmail.com

Beatriz Y. Benetti [e]

beatriz.yuri.silva@usp.br

[a] Departamento de Geologia, Centro de Ciências Exatas e da Terra, Universidade Federal do Rio Grande do Norte, Natal, RN 59078-970, Brazil

[b] School of Earth and Planetary Sciences, The Institute of Geoscience Research (TIGeR), Curtin University, GPO Box U1987, Perth, WA 6845, Australia

[c] Instituto de Geociências, Universidade de São Paulo, São Paulo, SP 05508-080, Brazil

[d] School of the Environment, Geography & Geosciences, University of Portsmouth, Portsmouth, PO1 3QL, UK

[e] Dipartimento di Scienze della Terra, Università degli Studi di Torino, via Valperga Caluso 35, 10125 Torino, Italy

ABSTRACT

Mineral assemblages that are diagnostic of ultrahigh-temperature (>900°C) metamorphism are generally restricted to Mg- and Al-rich rocks. However, in many metamorphic terrains such compositions do not occur, and the rocks are dominated by orthogneisses that typically contain high-variance mineral assemblages that are not diagnostic of particular pressure–temperature (*P–T)* conditions. Here we use whole-rock and mineral chemistry, thermodynamic phase equilibrium modelling, and zircon U–Pb–Hf isotopic data to constrain the *P–T*–time history of granulites from the Socorro-Guaxupé Nappe of the Southern Brasília Orogen. These rocks occur as part of a stack of Neoproterozoic nappes that were assembled during the formation of West Gondwana. Based on phase equilibrium modelling, the peak assemblage in a garnet-bearing felsic granulite (ortho- and clinopyroxene, garnet, K-feldspar, plagioclase, quartz, ilmenite, and silicate melt) records pressures of around 11.5 kbar and temperatures of ~1000°C, consistent with the high-Al content of orthopyroxene. The retrograde path records a small decrease in pressure to 9 kbar marked by orthopyroxene replacing garnet and the exsolution of magnetite from ilmenite followed by near-isobaric cooling that led to the development of coronas of hornblende around pyroxene due to crystallization of the last vestiges of melt. Zircon cores yielding U–Pb ages of *ca.* 625 Ma are interpreted as dating close-to-peak conditions during high-temperature metamorphism. In one sample, zircon rims and 'soccer ball' zircon neoblasts both have high U contents and yield ages of *ca.* 615 Ma, interpreted to mark the onset of melt crystallization. In two other samples, low-U rims and 'soccer ball' zircons grains yield ages of *ca.* 600-595 Ma, interpreted to date the end of melt crystallization. These data reveal a protracted regional metamorphic event in which the lower crust remained at granulite-facies conditions for at least 30 Myr during collision and assembly of West Gondwana.

Keywords: ultra-high temperature (UHT) metamorphism, *P–T*–t path, phase equilibrium modelling, petrochronology, Brasília Orogen

1 INTRODUCTION

Ultrahigh temperature (UHT) metamorphism is the most thermally-extreme type of crustal metamorphism, characterized by temperatures in excess of 900°C (Harley, 1998). There is widespread evidence that these metamorphic conditions have been generated repeatedly in time and space (e.g. Brown, 2007; Brown and Johnson, 2018; Clark et al., 2011; Harley, 2008; Kelsey, 2008; Korhonen et al., 2014). UHT metamorphism is most readily recognized via the presence of diagnostic stable mineral associations, such as sapphirine–quartz, orthopyroxene–sillimanite–quartz–melt, osumilite–garnet (Harley, 2008). However, these diagnostic mineral assemblages occur only in relatively rare MgO- and Al_2O_3-rich protoliths, raising the question of how UHT metamorphism can readily be identified in more common protoliths, such as felsic and mafic granulites with granitic and basaltic bulk-compositions, respectively. Partial melting is widespread in most rock compositions under UHT conditions, and the separation and extraction of this melt is critical to the preservation of peak metamorphic mineral assemblages in the lower continental crust (Baldwin et al., 2005; Moraes et al., 2002; White and Powell, 2002). Any melt remaining as the rock cools will crystallize and release H_2O, triggering retrograde re-equilibration and overprinting of the peak paragenesis by lower-temperature hydrous minerals, hampering temperature estimates based on conventional thermobarometry, as well as slow cooling, which makes cation exchange possible (Clark et al., 2011; Fitzsimons and Harley, 1994; Moraes et al., 2002; Pattison and Bégin, 1994; White and Powell, 2002).

Thermodynamic phase equilibrium modelling of bulk-rock compositions can be used to recover peak metamorphic conditions from UHT granulites that no longer preserve peak mineral compositions (Kelsey and Hand, 2015). Although activity–composition models appropriate for the anatexis of aluminous rocks (metapelites and metagreywackes) that produce haplogranitic liquids have been available for some time (Holland and Powell, 2001; White et al., 2007), it is only relatively recently that models dealing with high-temperature and high-pressure pyroxenes, amphiboles and K_2O-poor tonalitic to trondhjemitic melt have become available (Green et al., 2016), allowing quantitative thermodynamic modelling of partial melting and metamorphism in felsic and mafic granulites under UHT conditions.

Conventional thermobarometric calculations on felsic and mafic garnet granulites in the basal portion of the Socorro-Guaxupé Nappe, Minas Gerais, southeastern Brazil, have consistently yielded

UHT peak metamorphic conditions (Campos Neto and Caby, 2000; Del Lama et al., 2000, 1994; Moraes et al., 2015). Rocha et al. (2018, 2017) also have shown UHT conditions using Al-in-orthopyroxene thermobarometry, while Tedeschi et al. (2018) obtained these conditions using the Ti-in-zircon thermometer. In addition, geochronology were being done in the area without textural and chemical context, and given a large range for metamorphic peak ages, from 650 to 630 Ma (e.g. Braga, 2002; Campos Neto and Caby, 2000; Fetter et al., 2001; Salazar-Mora et al. 2014). More recently, an in situ geochronological (U-Pb) coupled with geochemical (REE) approach was conducted in zircon and monazite (Rocha et al., 2018, 2017; Tedeschi et al., 2018), showing a narrower range for the metamorphic peak (630-625 Ma) and putting the younger ages (*ca*. 600 Ma) in petrological context as associated with the crystallisation of melt. Here, we use the mineral chemistry, whole-rock geochemistry, mineral thermobarometry, phase-equilibrium pseudosection modelling, and U–Pb–Hf–REE zircon compositions to more precisely quantify the *P*–*T*–*t* history of the Socorro-Guaxupé granulites during Neoproterozoic metamorphism, targeting the metamorphic peak, the onset and end of melt crystallization, with consequences for the assembly of Gondwana and the gradual changes of Earth's tectonic processes.

2 GEOLOGICAL SETTING

The Socorro-Guaxupé Nappe is part of a stack of nappes in the Southern Brasília Orogen (Figure 1A), which formed during the assembly of West Gondwana by Neoproterozoic collision of a passive margin at the edge of the São Francisco plate with the active margin of the Paranapanema plate (Brito Neves et al., 1999; Brito Neves and Fuck, 2013; Campos Neto, 2000). The southernmost part of the Brasília Orogen is subdivided into three domains: an inner domain consisting of the Socorro-Guaxupé Nappe, which includes high-grade rocks formed in the root of the Paranapanema plate magmatic arc (Campos Neto and Caby, 2000, 1999); a central domain comprising the Andrelândia Nappe System, consisting of subducted high-*P* continental rocks of the São Francisco plate (Campos Neto et al., 2010; Campos Neto and Caby, 2000, 1999; Motta and Moraes, 2017; Trouw et al., 2000); and an external domain representing the continental passive margin of the São Francisco plate, which includes rocks of the Carrancas Nappe and Lima Duarte Nappe Systems (Campos Neto et al., 2004).

The Andrelândia Nappe System is composed of supracrustal rocks metamorphosed under amphibolite to high-pressure granulite conditions, comprising three major allochthons in an inverted metamorphic pattern (Campos Neto and Caby, 1999; Motta and Moraes, 2017). The metamorphic peak and migration of the nappe system was restricted to the interval 635 to 600 Ma-(Coelho et al., 2017; Frugis et al., 2018; Motta and Moraes, 2017), whereas the beginning of continental collision must have occurred at *ca.* 670 Ma (Frugis et al., 2018; Reno et al., 2009).

The Socorro-Guaxupé Nappe is an allochthonous high-grade metamorphic terrane dominated by granulites and migmatites (Campos Neto and Caby, 2000; Iyer et al., 1996; Rocha et al., 2018, 2017; Tedeschi et al., 2018), and comprises two main domains separated by Archean–Paleoproterozoic orthogneisses (Cioffi et al., 2016a, 2016b). The northwestern Guaxupé Domain represents the deeper crustal levels where granulites and diatexites are dominant (Figure 1B), whereas metatexites and extensive igneous bodies are more common in the southeastern Socorro Domain, where rocks decrease in grade southwards to amphibolite-facies conditions. In both domains, peak of metamorphism is dated at between 650 and 625 Ma (Campos Neto et al., 2004; Campos Neto and Caby, 2000; Fetter et al., 2001; Martins et al., 2009; Rocha et al., 2018, 2017; Salazar-Mora et al., 2014; Tedeschi et al., 2018). Pre-metamorphic magmatism is recorded over a protracted period from *ca.* 800 to 640 Ma (see Rocha et al., 2018 and references therein). ℇNd and ℇHf show systematically negative values with depleted mantle model ages ranging from 2.3 to 1.6 Ga (Janasi, 2002; Rocha et al., 2018; Salazar-Mora et al., 2014; Tedeschi et al., 2018).

This study focusses on the granulitic base of the Guaxupé Domain, which mainly comprises felsic granulites of acid to intermediate composition that are interlayered with ortho- and clinopyroxene-bearing mafic granulites and sillimanite- and spinel-bearing aluminous (metapelitic) granulites. Also present are intrusive charnockite bodies that are oriented both parallel to, and discordant with, the gneissic banding. Four samples were selected for chemical analysis and/or thermodynamic modelling, comprising two banded garnet-bearing felsic granulites (VAB01 and VAB19), a garnet-bearing felsic diatexite (RGM55) and a garnet-bearing mafic granulite (PAR03).

3 METHODS

3.1 Mineral and whole rock chemistry

Back-scattered electron imaging (BSE) and energy-dispersive X-ray spectroscopy (EDS) used a TESCAN MIRA3 Field-Emission Scanning Electron Microscope (FESEM) at the Microscopy & Microanalysis Facility, John de Laeter Centre, Curtin University, Australia, with a 15 mm working distance and accelerating voltage of 20 kV. Wavelength-dispersive spectrometry (WDS) analyses were performed with a JEOL JXA-8230 Hyperprobe at the Electron Microprobe Facility, Universidade Estadual Paulista (UNESP), Brazil, using a focused beam at 15 kV and 20 nA with 10 μm spot size for all minerals other than clinopyroxene, for which a 1 μm spot size was used due to the presence of closely-spaced exsolution lamellae of clinoenstatite. The analyses were recalculated using the AX software (https://www.esc.cam.ac.uk/research/research-groups/holland/ax). Analyses are given in Table S1 (Supporting information).

Compositional profiles were made across grains of garnet, pyroxene and feldspar in the two garnet-bearing felsic granulite samples (VAB01 and VAB19) and the garnet-bearing mafic granulite (PAR03). Biotite inclusions in garnet were analyzed in sample VAB01. Original (*i.e.* pre-exsolution) compositions of clinopyroxene in the felsic granulites were calculated by reintegration of the clinoenstatite lamellae and host clinopyroxene using average mineral compositions for each phase (n = 18 for both) weighted according to their relative proportions estimated from BSE images.

Garnet trace element analyses were performed using a Thermo Scientific iCAP Q ICP-MS coupled to a New Wave UP 213 nm laser ablation system at the NAP Geoanalítica, Institute of Geosciences at the University of São Paulo (IGc-USP), Brazil. Garnet was analyzed with 65 μm spot size, a laser fluence of 5.52 J/cm^2, and a repetition rate of 10 Hz. External calibration was performed relative to NIST 610 glass and the USGS BCR-2G basaltic glass reference material was analyzed as a secondary standard during analyses. Si and Ca determined by electron microprobe were used as internal standards. Results are presented in Table S2.

Bulk rock compositions were determined by X-ray fluorescence analysis using a Philips PW2400 at the NAP Geoanalítica, Brazil using a fused glass discs, following the methodology described by Mori et al. (1999). Trace elements, including rare earth elements (REE), were analyzed in decomposed powders, by microwave oven acid digestion (HF and HNO_3), by inductively coupled plasma mass spectrometry (ICP-MS) using a Thermo Scientific iCAP Q also located at IGc-USP, following the methodology described by Navarro et al. (2008). The results are presented in Table S3.

3.2 Phase equilibrium modelling

Phase equilibrium modelling of garnet-bearing felsic granulite (samples VAB01 and VAB19) and garnet mafic granulite sample PAR03 was performed in the ten-component NCKFMASHTO system (Na_2O–CaO–K_2O–FeO–MgO–Al_2O_3–SiO_2–H_2O–TiO_2–O_2) using THERMOCALC (Powell and Holland, 1988) version 3.45i, with the following activity–composition models: silicate melt (L), clinopyroxene (augite – aug) and hornblende (hb) from Green et al. (2016); garnet (g), orthopyroxene (opx), ilmenite (ilm) and biotite (bi) from White et al. (2014a); K-feldspar (ksp) and plagioclase (pl) from Holland and Powell (2003); magnetite (mt) from White et al. (2002). Rutile (ru), quartz (q) and aqueous fluid (H_2O) are considered pure phases. Calculations are confined to a *P*–*T* window of 7–13 kbar and 800–1050°C. Mn has a negligible effect on phase stability at high-*T* (White et al., 2014b) and was excluded from the model system. The bulk compositions used in the pseudosections (expressed as mol. % oxides) are given in Table 1. No modelling was attempted for diatexite sample RGM55 because the large volume of leucosome precludes accurate estimation of an appropriate bulk composition.

In order to estimate the likely H_2O content of felsic granulite VAB01 and VAB19 during high-*T* metamorphism, a *T*–X_{H_2O} pseudosection was calculated at a pressure of 10 kbar (approximate peak *P* for this rock – see below), where X_{H_2O} ranges from 0.01 to 5 mol. %. The H_2O content of 1 mol. % was chosen such that between 5% and 20% melt might be predicted, consistent with the field observations (Figure S1 – Supporting information). *P*–*X* pseudosections calculated at a temperature of 900°C (approximate peak *T* for this rock – see below) were used to constrain Fe_2O_3 contents at the metamorphic peak (expressed as O in the pseudosection calculations). An $X_{Fe_2O_3}$ value of 1 mol. % was chosen such that

ilmenite and magnetite (but not rutile) were stable, which matches the oxide phases observed in the rocks (Figure S2 – Supporting information).

P–*T* pseudosections for the garnet mafic granulite were constructed using two different values for the H_2O content, one with the measured loss-on-ignition value (0.01 wt. %) and another with an assumed 1 mol. % of water. Assemblage fields in the P–$X_{Fe_2O_3}$ pseudosection for this rock do not show significant variability in the oxide phases, thus an $Fe^{3+}/\Sigma Fe$ ratio of ~0.2 was assumed, which is similar to the observed value in intrusive igneous rocks associated with arc magmatism (Evans, 2012).

3.3 U–Pb geochronology

Zircon grains were extracted from the garnet-bearing felsic granulite and diatexite samples (VAB01, VAB19 and RGM55) via traditional methods of disaggregation, magnetic and heavy liquid separation. The grains were mounted together with primary and secondary standards and NIST-610 glass. After polishing, the mounts were carbon-coated and imaged by cathodoluminescence (CL) using a TESCAN MIRA3 FESEM. The mounts were cleaned and covered with a 40 μm gold coat prior to U–Pb isotopic analysis using the Sensitive High Resolution Ion Microprobe (SHRIMP II). All this equipment is housed in the John de Laeter Centre at Curtin University.

SHRIMP II was operated at a mass resolution of 5,000, with a primary beam current of 2 nA and beam diameter of 20 μm, and a 6-scan cycle was used during analysis (de Laeter and Kennedy, 1998; Kennedy and de Laeter, 1994). NIST-610 glass was used to calibrate the position of the ^{204}Pb peak. CUYZ (Curtin internal laboratory standard, with an age of 568.55 Ma) was used as primary standard and OGC (Stern et al., 2009) as a secondary standard. Data were processed using the SQUID II and Isoplot 3.75 (Ludwig, 2009; 2003) software with the correction of measured isotopic ratios for common Pb based on Stacey and Kramers (1975). External spot-to-spot errors on zircon U–Pb calibration sessions were <1%, which reflects the long-term performance of the SHRIMP II. The $^{207}Pb/^{206}Pb$ age of the secondary standard determined during the analytical session was 3469.9 ± 7.6 Ma, which is within error of the published age (3465.4 ± 0.6 Ma; Stern et al., 2009). U–Pb data are presented in Table S4. Uncertainties cited for individual spot analysis include errors from counting statistics, errors from the common Pb

206 correction and U-Pb calibration errors based on reproducibility of measurements of the standard are
207 given as 2σ if not indicated in the text. In the sample VAB01, 20 spot analysis were done in 19 grains;
208 sample VAB19, 11 spot analysis in 11 grains and the sample RGM55, 17 spot analysis were done in 14
209 grains. All the analysis were considered in the calculations, exceptions are explained in the text.

210 **3.4 Zircon trace element and Lu–Hf isotope analysis**

211 Trace elements and Lu–Hf isotopes and complementary U–Pb data of zircon were collected using
212 Split-Stream Laser Ablation with Inductively Coupled Plasma Mass Spectrometry (LASS–ICP–MS) on an
213 ASI Resolution M-50 with a 193-nm wavelength Ar–F excimer laser with an Agilent 7700 mass
214 spectrometer at the GeoHistory Facility, John de Laeter Centre, Curtin University. Laser fluency was 2
215 J/cm^{-2}, at a repetition rate of 10 Hz and spot size of 50 μm. Reference material NIST-610 was used as
216 primary standard and OGC (Stern et al., 2009), GJ-1 (Jackson et al., 2004) and Plešovice (Sláma et al.,
217 2008) as secondary standards. Data were processed, corrected for down-hole fractionation and
218 instrumental drift using Iolite 3.4 software (Paton et al., 2011). The same samples analyzed by SHRIMP
219 were used to analyze trace elements, Lu and Hf isotopes and complementary U-Pb. Figure S3 shows a
220 comparison of LASS–ICP–MS and SHRIMP U-Pb data. When possible, Lu-Hf calculations were done using
221 the ages obtained by SHRIMP. Data are presented in Tables S5, S6 and S7.

222 **4 RESULTS**

223 **4.1 Petrography and bulk rock chemistry**

224 **4.1.1 Garnet-bearing felsic granulite (samples VAB01 and VAB19)**

225 The garnet-bearing felsic granulite has a well-developed compositional and textural layering
226 (Figure 2A), comprising medium- to coarse-grained anhydrous leucosome, a fine- to coarse-grained
227 residuum and a poorly developed selvedge of hornblende at the margins of the leucosome (Figure 2B).
228 The layering is typically closely-spaced and bulk compositions determined for these rocks are mixtures
229 of leucosomes, residuum and selvedge.

230 The residuum contains the peak paragenesis garnet (5–10%), orthopyroxene (5–7%),
231 clinopyroxene (3–5%), plagioclase (40–50%), perthite (5–10%), quartz (20–25%) and ilmenite (<5%).

Quartz inclusions in garnet, thin quartz films along the contacts between garnet and pyroxene (Figure 2C) and cuspate grains of orthoclase surrounding plagioclase (Figure 2D) are interpreted as pseudomorphs after trapped anatectic melt (Holness et al., 2011; Waters, 2001), showing that it was part of the peak paragenesis. Coronae of clinopyroxene locally surround orthopyroxene. Hornblende is the only hydrous mineral in the rock matrix and replaces pyroxenes (Figure 2E), whereas rounded grains of biotite (but not hornblende) occur as inclusions in garnet. The oxide phases comprise striped intergrowths of ilmenite and Ti-magnetite (Figure 2F).

The leucosome contains garnet, orthopyroxene, clinopyroxene, plagioclase, perthite, quartz and hornblende (Figure 2B). Porphyroblasts or symmetric porphyroclasts of mafic phases, mainly orthopyroxene and garnet, occur locally in this domain (Figure 2A). The volume of leucosome in the rock can reach 15 %. Clinopyroxene in both leucosome and residuum contains exsolution lamellae of clinoenstatite (Figure 2F).

The analyzed samples (VAB01 and VAB19) have similar contents of major elements (*e.g.* SiO2 between 61.7 and 63.5 wt.%) and match the compositions of intermediate granulites reported from the western part of the Guaxupé Domain (Del Lama et al., 1998), plotting between the fields of diorite and granodiorite (Figure 3A) in a TAS diagram (Middlemost, 1994). Samples VAB01 and VAB19 have similar chondrite-normalized bulk-rock REE abundances (Figure 3B) with a fractionated trend from more-abundant light REE (LREE) towards less-abundant heavy REE (HREE). This fractionation is stronger in sample VAB19 (La_N/Yb_N = 19.7) than in VAB01 (La_N/Yb_N = 7.9). Both samples are strongly depleted in Th and U and enriched Ti (Figure 3C), compared to average continental crust (Wedepohl, 1995).

4.1.2 Diatexite (sample RGM55)

The diatexite contains > 60% leucosome, within which are rafts of residuum. The rafts are fine-grained and composed of garnet (<5%), orthopyroxene (5–10%), clinopyroxene (3–5%), plagioclase (35–40%), perthite (10–15%), quartz (25-30%) and ilmenite. The leucosome is composed of medium- to coarse-grained orthopyroxene, clinopyroxene, perthite, plagioclase and interstitial quartz, and has a syenite composition (Figure 3A), similar to the group of acid granulites from the western part of the

domain (Del Lama et al., 1998). Garnet is scarce, comprising less than 1% of the leucosomes. Perthite megacrysts generally contain inclusions of rounded quartz and subhedral plagioclase. Pyroxene grains are locally replaced at their margins by late biotite and/or biotite–oxide intergrowths (Figure 2G). Accessory minerals include large crystals of zircon, apatite and allanite (Figure 2H).

The bulk REE patterns show pronounced enrichment in LREE (Figure 3B) relative to HREE (La_N/Yb_N = 149.9). The sample rock is enriched in K, Rb, Th, LREE, Zr and Hf relative to average continental crust (Wedepohl, 1995), but depleted in Sr (Figure 3C), a pattern that is distinct from the felsic garnet granulite samples.

4.1.3 Garnet-bearing mafic granulite (sample PAR03)

The garnet-bearing mafic granulite exhibits a peak metamorphic mineral assemblage of garnet (<2%), orthopyroxene (15–20%), clinopyroxene (25–30%), plagioclase (40–55%), quartz (<5%), ilmenite (3%) and magnetite (3%). It has a fine-grained granoblastic texture with a poorly-developed foliation and does not contain any hydrous phases (Figure 2I). Rare millimetric patches of leucosome are composed of plagioclase and quartz with a tonalitic–dioritic composition and are interpreted to represent crystallized anatectic melt. Rare orthopyroxene porphyroblasts contain thin exsolution lamellae of clinopyroxene, and are locally surrounded by a discontinuous corona of the same mineral. Its composition is more basic (~ 47.4 wt% of SiO_2) than the basic granulites from the western part of the domain (Figure 3A).

4.2 Mineral chemistry

4.2.1 Garnet

Grains of garnet from the garnet-bearing felsic granulite show no evidence for pronounced major element zonation (Figure 4A and C). Values of X_{Mg} (= atomic Mg/[Mg + Fe^{2+}]) in sample VAB01 on grains up to 7 mm in size are higher than in sample VAB19 (0.37 versus 0.32), but the grossular content (X_{gr} = Ca/[Ca + Mg + Fe^{2+} + Mn]) in both samples is similar (X_{gr} = 0.12–0.14). Garnet in the garnet-bearing mafic granulite is homogeneous in composition (X_{Mg} = 0.24 and X_{gr} = 0.18–0.19), with lower X_{Mg} and higher grossular contents than garnet in the felsic granulite (Figure 4E).

284 Garnet from sample VAB01 exhibits three different REE patterns (Figure 4B). Crystals larger
285 than ~ 7 mm have cores (core 1) that are relatively depleted in HREE, and exhibit a moderate degree of
286 fractionation, with preferential concentrations in MREE over HREE (Gd_N/Yb_N = 7.1). The intermediate
287 portions of crystals larger than ~ 7 mm, as well as cores of garnet grains smaller than ~ 7 mm (core 2),
288 have flatter HREE patterns (Gd_N/Yb_N ~ 0.9). The garnet rims are slightly depleted in HREE (Gd_N/Yb_N ~
289 0.7) relative to core 2 analyses in all crystals. All garnet variants in this sample have similar LREE–MREE
290 patterns, and have small negative Eu anomalies (Figure 4B).

291 The REE compositions of garnet from sample VAB19 show no significant differences between
292 rims and cores (Figure 4D). Most notably, the grains show a significant fractionation with preferential
293 incorporation of HREE over MREE (Gd_N/Yb_N ~ 0.2).

294 **4.2.2 Pyroxenes**

295 Orthopyroxene shows minor variations in X_{Mg} in the garnet-bearing felsic granulite (0.57–0.61
296 in VAB01 and 0.53–0.56 in VAB19) and in the garnet mafic granulite (X_{Mg} 0.49–0.52 in PAR03). However,
297 significant variations in tetrahedral Al (Al^T = elemental Si + Al – 2) are observed, with cores relatively
298 depleted in Al. Sample VAB01 has Al^T between 0.033 and 0.063, whereas sample VAB19 has Al^T between
299 0.030 and 0.050. Such variations are also observed in the garnet mafic granulite (PAR03), in which Al^T
300 is 0.025–0.044.

301 Clinopyroxene within the garnet-bearing felsic granulite has an average X_{Mg} of 0.69 and 0.85
302 atoms per formula unit (apfu) Ca (based on 6 oxygens). The exsolution lamellae of clinoenstatite have
303 lower X_{Mg} (~ 0.54), with almost no Ca and Al^T ~ 0.075. Based on BSE images, the clinopyroxene grains
304 are estimated to contain around 10% clinoenstatite lamellae, equating to an X_{Mg} of 0.66 and 0.76 apfu
305 Ca in the original high-*T* clinopyroxene. In the garnet mafic granulite, clinopyroxene has an X_{Mg} of 0.63
306 and contains 0.84 apfu Ca.

307 **4.2.3 Plagioclase**

In the garnet-bearing felsic granulite, plagioclase shows no pronounced compositional zoning and has an average composition of $An_{58–61}$. Conversely, plagioclase in the garnet mafic granulite has an intense optical zonation, with cores more enriched in anorthite ($An_{50–70}$) than rims ($An_{40–45}$).

4.2.4 Biotite

Biotite inclusions in garnet from the garnet-bearing felsic granulite sample VAB01 have X_{Mg} of 0.7 and Ti contents between 0.133 and 0.286 apfu, based on 11 oxygens.

4.3 Conventional thermobarometry

Compositions of coexisting garnet and orthopyroxene were used to estimate *P*–*T* conditions using garnet–orthopyroxene thermobarometry corrected for late Fe–Mg exchange (Pattison et al., 2003). The association orthopyroxene–clinopyroxene–garnet–quartz–plagioclase was used to estimate pressure and temperature through the average *P*–*T* mode of THERMOCALC – version 3.45i (Holland and Powell, 1998) (see Table 2).

Metamorphic conditions estimated for the garnet-bearing felsic granulite sample VAB01 using the average *P*–*T* calculations suggest ultrahigh temperatures of 1009 ± 144°C at pressures of 11.5 ± 3.0 kbar. The Al-solubility-based thermobarometer of Pattison et al. (2003), using the model 2 of the RCLC program and mineral modes observed in the petrography, yielded similar temperatures (1020°C), but higher pressures (14.4 kbar). However, at a fixed pressure of 11 bar, temperatures of 936°C are calculated, within uncertainties of the THERMOCALC calculations.

Calculated conditions for the garnet mafic granulite overlap with those for the garnet-bearing felsic granulite within error. The average *P*–*T* calculations yielded 936 ± 186°C at 10.2 ± 2.2 kbar, whereas the Al-solubility-based thermobarometer yielded a temperature of 919°C and pressure of 11.0 kbar.

4.4. Phase Equilibrium Modelling

A *P*–*T* pseudosection for garnet-bearing felsic granulite sample VAB01 with ~1 mol.% H_2O is shown in Figure 5. Within the modelled *P*–*T* window, the solidus occurs between 840°C at lower and

higher *P* and 880°C at intermediate *P*. Orthopyroxene is stable at relatively low *P*, and garnet at relatively high *P*, with both minerals coexisting within a broad field at pressures of 8–12 kbar. Clinopyroxene is stable everywhere except at the highest pressures and lowest temperatures. The hornblende-out line is strongly dependent on temperature, ranging from ~860°C at 7 kbar to 930°C at 11–13 kbar. Magnetite is only stable at low pressures (<8–10 kbar). K-feldspar stability is predicted up to temperatures of 960°C at lower *P* to 1040°C at higher *P*. Quartz, plagioclase and ilmenite are ubiquitous, and biotite is not predicted to be stable. The field containing the inferred peak paragenesis (clinopyroxene–orthopyroxene–garnet–ilmenite–K-feldspar–plagioclase–quartz–melt) is predicted to be stable between 880 and 1030°C at 8.6 to 12.1 kbar. The quantity of melt in this field varies from 5 to 20 mol.% and the compositional isopleths of tetrahedral Al in orthopyroxene range from 0.049 to 0.067 cations in the formula unit based on six oxygens (Figure 5). A similar geometry is observed in a pseudosection calculated for the other garnet-bearing felsic granulite (VAB19), where the peak mineral association is present over the same range of temperature as VAB01 (880 to 1030°C) but spanning a lower range of pressure from 8.6 to 11.2 kbar (Figure S4).

The changing modal proportion of phases as a function of temperature was calculated at a fixed pressure of 10 kbar (Figure 5B) to understand the behaviour of phases during the cooling path. Near to the metamorphic peak conditions, around 1000°C, the modes of garnet and K-feldspar are very low, increasing towards lower temperatures. On the other hand, at lower temperature, plagioclase content tends to decrease. Hornblende must be present at temperatures lower than 925°C, and melt would be crystallized at temperatures around 875°C. If the rock were heated over the metamorphic peak conditions, garnet and K-feldspar would be consumed, and the amount of plagioclase would increase.

The *P*–*T* pseudosection for the garnet mafic granulite with 1% H_2O is shown in Figure 6A. The solidus occurs at temperatures between 830 and 880°C and has a positive d*P*/d*T* at relatively low *P,* but becomes negative at pressures above the disappearance of orthopyroxene at around 9 kbar. The hornblende-out line is broadly parallel with the solidus, but occurs at higher temperatures of between 870 and 900°C. The stability fields of magnetite, garnet and orthopyroxene are strongly dependent on pressure. Magnetite and orthopyroxene are stable at lower pressures, magnetite below 8.2–9.4 kbar and

orthopyroxene below 8.1–10.4 kbar. Garnet is predicted at pressures above 7.6–9.8 kbar. At temperatures lower than the solidus hornblende and quartz are always present, whereas in the hornblende-free region quartz is absent at pressures below ~9.5 kbar. Rutile occurs only at pressures above 12 kbar. Plagioclase, clinopyroxene and ilmenite are present throughout the *P*–*T* range considered. The paragenesis quartz–garnet–ilmenite–orthopyroxene–clinopyroxene–plagioclase–leucosome, interpreted to have been present at the metamorphic peak, is calculated to occur between 900 and 1030°C, at pressures of 9 to 10.4 kbar, within a field no wider than 0.5 kbar. The modal proportion of melt calculated within this field varies from 5 to 20% (Figure 6A).

In the *P*–*T* pseudosection for the garnet mafic granulite with minimal water (Figure 6B; H_2O = 0.01%), the solidus and hornblende-out lines coincide and occur at higher temperatures of between 860 and 900°C. Garnet is stable at pressures above 7.4 kbar and orthopyroxene is stable at pressures below 8.8–10.7 kbar. Magnetite and rutile are not predicted within the *P*–*T* window considered. Plagioclase, clinopyroxene and ilmenite are present throughout, and quartz is stable at all *P*–*T* conditions, except at the lowest *P* and *T*. The peak paragenesis occurs at temperatures above 880°C and at pressures between 8.0 and 10.7 kbar, within which melt proportions are <1% (Figure 6B).

4.5 Zircon U–Pb Geochronology

Samples VAB01 and VAB19 both contain two types of zircon crystals with different shapes and internal CL domains (Figure 7). One type comprises subhedral prismatic crystals (~2:1 aspect ratio) with rounded terminations, and dark luminescent cores with narrow to broad oscillatory-zoning, which are surrounded by bright-CL rims that are homogeneous or have sector-zoning. The cores of this zircon type yielded $^{206}Pb/^{238}U$ dates ranging from *ca.* 705 to 631 Ma (Figure 8A). In both samples, the cores have similar Th/U ratios with an average value of 0.6 and contents of both U and Th that are always higher than 70 ppm (Figure 8D). A second group of crystals is rounded and shows sector zoning ('soccer ball' type), with bright to moderate CL response, occasionally with darker xenocrystic oscillatory-zoned cores (Figure 7). The bright CL rims of the prismatic zircon grains (3 in VAB01 and 5 in VAB19) and the soccer ball crystals (11 in VAB01 and 3 in VAB19) appear to belong to the same age population and

yielded weighted mean $^{206}Pb/^{238}U$ dates of 593.8 ± 8.5 Ma (MSWD = 3.5; n = 14) in VAB01 and 598.5 ± 4.6 Ma (MSWD = 2.0; n = 8) in VAB19 (Figure 8A and B). Their Th/U ratios are higher than in the oscillatory-zoned cores of prismatic grains and are commonly >1.0 (Figure 8D). This group is variably depleted in U compared to the cores of the first zircon type and may also be depleted in Th (Figure 8D).

The diatexite (RGM55) contains three morphological types of zircon crystal (Figure 7). These include subhedral prismatic grains with rounded terminations, similar to those in VAB01 and VAB19, but with cores that are predominantly sector-zoned or disturbed-zoned with only a few grains exhibiting broad-oscillatory patterns. These grains have rims that are darkly luminescent and contain relatively high U contents (from 242 to 126 ppm, with average of 204 ppm). Soccer ball zircons are also present, but have a darker CL response and higher U content than those in VAB01 and VAB19 (Figure 8D). A third group comprises anhedral zircon grains characterized by sector-zoning. In this sample, the prismatic sector-zoned cores yielded a weighted mean $^{206}Pb/^{238}U$ date of 624.8 ± 3.4 Ma (MSWD = 2.0; n = 6; Figure 8C) and an average Th/U ratio of 0.56 (Figure 8D), although one spot from a broad oscillatory-zoned core yielded an older $^{206}Pb/^{238}U$ date of 639 ± 18 Ma, this data excluded from the calculations, as this data shows older age with a different texture. Complementary U–Pb data obtained by LASS–ICP–MS in grains with broad oscillatory-zoned or some sector-zoned revealed the oldest $^{206}Pb/^{238}U$ dates that scattered from 660.9 ± 7.1 to 631.4 ± 8.5 Ma (Figure 8C) and have Th/U ratios similar to the prismatic sector-zoned cores (Figure 8D). The rims, soccer ball and anhedral grains have lower Th/U ratios (from 0.692 to 0.047 with an average of 0.26; Figure 8D) and lower Th contents relative to sector-zoned cores, and yielded a younger weighted mean $^{206}Pb/^{238}U$ date of 615.8 ± 3.4 Ma (MSWD = 1.6; n = 8; Figure 8C), although two spots in anhedral grains, yielded younger $^{206}Pb/^{238}U$ dates of 599 ± 16 Ma (Th/U = 0.22) and 594 ± 14 Ma (Th/U = 0.16), which together yielded a concordia age of 597.3 ± 5.1 Ma (MSWD = 1.6; n = 2; Figure 8C).

4.6 REE and Lu–Hf in zircon

The same samples (VAB01, VAB19 and RGM55) analyzed by SHRIMP were analyzed for REE abundances and Lu–Hf isotopes by LASS–ICP–MS. The analyses were made in the five different zircon

412 domains differentiated on the basis of CL and U–Pb analysis: (i) oscillatory-zoned cores (VAB01 and
413 VAB19); (ii) sector-zoned to broad oscillatory-zoned crystals (RGM55); (iii) sector-zoned cores
414 (RGM55); (iv) soccer ball crystals and rims with high U (RGM55); and (v) soccer ball crystals and rims
415 with low U (VAB01 and VAB19).

416 Sample VAB01 shows three distinct zircon REE patterns (Figure 9A). The oscillatory-zoned
417 cores, which yielded the oldest dates of up to *ca.* 705 Ma, are moderately enriched in LREE relative to
418 chondrite, with weak Eu anomalies, and strongly enriched in HREE with concentrations up to 10^4 times
419 more than in chondrite (Figure 9A). The $^{176}Hf/^{177}Hf$ ratios are between 0.282223 and 0.282251 (Figure
420 9~~F~~D), equivalent to $\varepsilon Hf_{(t)}$ between –4.73 and –4.11, with an outlier value of 0.282325 ($\varepsilon Hf_{(t)}$ = –0.87).
421 The zircon rims are relatively depleted in La, have a pronounced positive Ce anomaly, a weakly negative
422 Eu anomaly, and a steeper HREE array, although the overall concentrations of HREE are lower than in
423 the oscillatory-zoned cores (Figure 9A). It is possible that these analyses represent a mixture between
424 rims and cores as laser pits from the LASS–ICP–MS are wider and deeper than the SHRIMP pits. The
425 soccer ball crystals, which yielded similar ages to the rims (593.8 Ma), have similar patterns of LREE
426 and MREE as the rims, but the HREE array is flat or exhibits a slight enrichment (Figure 9A). Zircon rims
427 and soccer ball grains have similar $^{176}Hf/^{177}Hf$ ratios, between 0.282245 and 0.282314 (Figure 9D),
428 equivalent to $\varepsilon Hf_{(t)}$ values of between –6.02 and –3.31.

429 Zircon from sample VAB19 shows broad similarities with zircon from sample VAB01 (Figure
430 9B). Oscillatory-zoned cores (up to *ca.* 700 Ma) are moderately enriched in LREE and MREE, with weak
431 Eu anomalies, and are strongly enriched in HREE (Figure 9B). The $^{176}Hf/^{177}Hf$ ratios (0.282231–
432 0.282239) of this group are similar to the oscillatory-zoned zircon cores in sample VAB01, and yield
433 $\varepsilon Hf_{(t)}$ values between –4.04 and –4.02 (Figure9D). A single analysis from a rim shows strong enrichment
434 in LREE, higher than in the oscillatory-zoned cores, HREE contents that are lower than the oscillatory-
435 zoned cores, with a negative Eu anomaly (Figure 9B). This rim yielded the lowest $^{176}Hf/^{177}Hf$ value of
436 0.281962 (Figure 9D), corresponding to the most negative $\varepsilon Hf_{(t)}$ (–15.9). Soccer ball crystals show the
437 same pattern as soccer ball grains from VAB01, with depletion in La, strongly positive Ce anomalies,
438 weakly negative Eu anomalies and flat HREE patterns (Figure 9B). The $^{176}Hf/^{177}Hf$ ratios are slightly

evolved compared to the oscillatory-zoned cores, between 0.282254 and 0.282271 (Figure 9D) and $\varepsilon Hf_{(t)}$ between –5.92 and –4.12.

In sample RGM55, the older broad oscillatory-zoned core domains, which range in age from 631 and 661 Ma, show both enrichment and depletion in LREE, with weakly to strongly positive Ce anomalies and negative Eu anomalies, and enrichment in HREE (Figure 9C). Zircon crystals from this sample are less radiogenic than in the other samples (VAB01 and VAB19), with $^{176}Hf/^{177}Hf$ ratios between 0.282148 and 0.282207, corresponding to $\varepsilon Hf_{(t)}$ values that range from –8.48 and –6.36 (Figure 9D).

The prismatic crystals from RGM55 with sector-zoned or disturbed zoned cores and ages of *ca.* 625 Ma show two contrasting LREE patterns, one moderately enriched in LREE and with weakly positive Ce anomalies and another that is depleted in LREE with strongly positive Ce anomalies. MREE and HREE distributions are similar in these two types and show negative Eu anomalies and a strong enrichment in the heaviest elements (Figure 9C). The $^{176}Hf/^{177}Hf$ ratios range from 0.282150 and 0.282181 (Figure 9 D), yielding $\varepsilon Hf_{(t)}$ values from –8.55 and –7.34.

The REE array in the anhedral and soccer ball grains from sample RGM55 (*ca.* 615 Ma) shows a spread in LREE concentrations and positive Ce anomalies that are less pronounced than in the sector-zoned cores, although an outlier is enriched in LREE and lacks any Ce anomaly (Figure 9C). The MREE shows negative Eu anomalies and there is a steeper enrichment in HREE. The $^{176}Hf/^{177}Hf$ ratios, between 0.282133 and 0.282201, give $\varepsilon Hf_{(t)}$ values between –9.71 and –7.04, which are similar to the other domains (Figure 9D).

The two youngest anhedral zircon grains (597 Ma) from sample RGM55 present similar M- and HREE patterns to the other groups, with negative Eu anomalies and enrichment in HREE (Figure 9C). Whereas one grain shows similar LREE behaviour to the other groups, the other shows an anomalous enrichment in LREE, which might represent a coeval growth in a different chemical domain, without the presence of plagioclase or amphibole, for example. Both grains have less radiogenic $^{176}Hf/^{177}Hf$ ratios (0.282133 and 0.282410) than the older domains (Figure 9D).

5 DISCUSSION

5.1 *P–T* path

The metamorphic *P–T* path of the base of Socorro-Guaxupé Nappe can be constrained by sample VAB01 due to its particular petrographic features. Biotite grains armored in garnet have rounded shapes and high Ti contents and X_{Mg} values. Therefore, partial melting may initially have been by reactions consuming biotite. Nevertheless, to reach the UHT conditions and preserve mineral assemblages, the rock is likely to have lost these first batches of melt (Clark et al., 2011; Kelsey and Hand, 2015; Vielzeuf et al., 1990), modifying its composition, and become less prone to thermal buffering. Thus, the metamorphic modelling calculated here cannot constrain the prograde metamorphic path.

According to the phase equilibrium modelling, continued melting would have been driven by breakdown of K-feldspar and garnet once the rock had been exhausted of hydrous minerals (Figure 5). The granulite is extremely depleted in Th and U and depleted in Rb relative to average continental crust (Figure 3), which is consistent with depletion by melt loss during granulite metamorphism. Whole-rock chemical data from orthogneiss from the Domain, which presents lower metamorphic conditions, shows higher contents of Th, U and Rb (Genco, 2014) compared to the orthogneiss from this work, which support the idea of depletion due to melt loss. A small enrichment in Sr relative to average continental crust might indicate that plagioclase was not a major reactant phase during partial melting of the granulite, which is suggested in the phase equilibrium modelling that predicts plagioclase would increase in model abundance after the metamorphic peak (Figure 5B).

The calculated pseudosection assemblage fields for the inferred metamorphic paragenesis in both the garnet-bearing felsic and mafic granulites overlap and are consistent with peak conditions of around 1000°C at pressures higher than 9 kbar (Figure 10). Calculations using the average *P–T* mode of THERMOCALC yielded similar conditions, as do *P–T* estimates based on the maximum Al-in-orthopyroxene of the garnet-bearing felsic granulite (Figure 10). The high-*T* homogenized the major elements in garnet, whereas trace elements were not, due to the low diffusion (Kohn and Penniston-Dorland, 2017) (Figure 4).

We suggest that the high-*T* retrograde evolution was associated with a small decrease in pressure to 9 kbar (Figure 10), as evidenced by orthopyroxene replacing garnet and the exsolution of magnetite from ilmenite (Figure 2). Thereafter, the rock followed a near-isobaric cooling path, remaining within the stability field of garnet, since coronas or other textures of garnet replacement are poorly developed. At temperatures close to the elevated (melt-depleted) solidus, hornblende began to crystallize at the edge of pyroxene, particularly in the leucosome, consistent with conditions of around 870°C and 8.5 kbar (Figure 10), which suggest re-hydration of pyroxene when the crystallized melt released water to the system.

5.2 Timescales of metamorphism

The geochronological data reveal at least four groups of ages that we suggest can be related to distinct periods of zircon crystallization – one related to early magmatism, one to prograde to peak metamorphism and two to melt crystallization (Figure 10). Although the garnet-bearing felsic granulite and the diatexite appear not to have had the same protolith, some comparisons can be made.

In samples VAB01 and VAB19, oscillatory-zoned zircon cores exhibit higher U and lower Th/U ratios than the rims or soccer ball crystals (Figure 8C), and have older ages, ranging from *ca.* 630 Ma up to 705 Ma. Sample RGM55 also shows older ages in oscillatory-zoned or sector-zoned cores of zircon that range between *ca.* 660 to 631 Ma. We suggest that the oldest dates from the three samples (VAB01, VAB19 and RGM55) may reflect the age of igneous crystallization of the protolith and do not have any relation to the metamorphism. Similar scattered magmatic ages were previously observed in other studies in the southern Brasília Orogen (Janasi, 1999, 2002; Martins et al., 2009; Salazar-Mora et al., 2014; Rocha et al., 2017; Rocha et al., 2018; Tedeschi et al., 2018). The U/Yb ratios of these zircon cores always show values higher than 0.1, which suggest a granitoid source with no relation to the oceanic crust (Grimes et al., 2015).

The zircon cores in sample VAB01 have higher concentrations of LREE and HREE and similar contents of MREE to garnet cores and rims in this sample, as shown in zircon/garnet REE partitioning diagrams (Figure 11A, C and E). Conversely, in sample VAB19 the zircon cores are enriched in LREE and

517 depleted in MREE and HREE relative to garnet (Figure 11G). To assess equilibrium relationships
518 between zircon and garnet we use the array plots proposed by Taylor et al. (2017), showing log
519 (D_{Yb}/D_{Gd}) vs. log (D_{Yb}) of every zircon analysis against all different garnet compositions in samples
520 VAB01 and VAB19. In the plots (Figure 11B, D and F), zircon core data from both samples (VAB01 and
521 19) are clustered, showing no clear trends, suggesting that these domains cannot have grown in
522 equilibrium with garnet, corroborated by the enrichment in HREE in zircon in the traditional D_{REE} plots
523 (Figure 11A, C and E).

524 In the diatexite (RGM55) subhedral prismatic zircon with sector-zoned or disturbed zoned cores
525 record a weighted mean date of 625.9 ± 3.5 Ma. Based on the bulk-rock REE composition of this sample
526 (which is enriched in LREE), its mineralogy (allanite-bearing and garnet-depleted), and the REE
527 composition of its constituent zircon (which shows pronounced positive Ce and negative Eu anomalies),
528 this sample is unlikely to have had the same protolith as the felsic garnet granulite. Thus, the date of *ca.*
529 625 Ma may represent the age of crystallization of the magmatic protolith, although a previously
530 mentioned oscillatory-zoned core yields older date (> 630 Ma). Another possibility is that the *ca.* 625
531 Ma date could represent recrystallization of inherited material or magmatic zircon, since this process
532 can result in expulsion of the pre-existing Pb, and resetting of the U–Pb system (Taylor et al., 2016).
533 Grains of this domain show a progressive loss of the original internal features, as commonly observed
534 in high-grade conditions (Taylor et al., 2016). SHRIMP analysis spot #13.2 shows the loss of original
535 internal features, showing a ghost oscillatory-zoned texture, as well as in spot #14.1, which shows a
536 disturbed zoning pattern of previous (Figure 7C). This age matches the timing of the metamorphic peak
537 in the Socorro-Guaxupé Nappe as determined in other studies (Rocha et al., 2017; Rocha et al., 2018;
538 Tedeschi et al., 2018), which also used petrochronological data to assign meaning to the ages.

539 The rims of most zircon crystals, soccer ball and shapeless zircon crystals in sample RGM55,
540 which yield a date of 615.8 ± 3.4 Ma, register the highest contents in U (up to 347 ppm) and lowest Th/U
541 ratios (~ 0.23) of the studied samples (Figure 8C). In comparison to their cores, they are depleted in Th
542 and have a wider range of LREE contents, suggesting that allanite, a sink for these elements (Hermann,
543 2002), including Th, was crystallizing at same time. This was made possible by the very high abundance

544 of LREE in the bulk composition which will stabilize allanite at such high temperature conditions
545 (Hermann, 2002). Other studies using U-Pb geochronology combined with trace elements in zircon and
546 monazite interpret this age (*ca.* 615 Ma) as the time of melt crystallization in the Guaxupé Domain
547 (Rocha et al., 2018, 2017). The data presented here also suggest this interpretation, where the zircon
548 may have begun to crystallize by the Zr saturation of the melt, at the same time as crystallization of
549 allanite. Thus, the date of *ca.* 615 Ma may represent a time closer to the onset of melt crystallization.

550 The rims and soccer ball zircon from samples VAB01 and VAB19 record the lowest contents of
551 U, the highest Th/U ratios and the youngest ages (Figure 8C). Major phases are more able to incorporate
552 U rather than Th (Yakymchuk et al., 2018), thus, without the presence of a Th-bearing phase, the Th/U
553 ratios in the melt tend to increase during crystallization. Therefore, this group may reflect the final
554 crystallization of the trapped melt (Figure 10), when the availability of U was low.

555 The D_{REE} for zircon–garnet from sample VAB01 for soccer ball crystals shows a flat pattern of
556 MREE and HREE when combined with core2 and rim garnet REE data (Figure 11C and E), but not when
557 they were normalized to the core of larger garnet grains (Figure 11A). Other than that, the data from
558 zircon rims show flat patterns of MREE and enrichment in HREE (Figure 11A, C and E), which may
559 indicate a mix with the core domain, as the spot size of the laser ablation is larger than the SHRIMP. The
560 garnet cores from smaller crystals or the intermediate domain of larger crystals and the garnet rims
561 from sample VAB01 better fit the zircon data, which show the same slope and trends as the experimental
562 data (Figure 11D and F). Thus, this behaviour implies that the low U zircon group from sample VAB01
563 grew in equilibrium with garnet, which is supported by the flat pattern of HREE in both minerals (Figure
564 4 and Figure 9), once both were competing to these elements.

565 The D_{REE} zircon–garnet plot for zircon rims and soccer ball crystals from sample VAB19 show M
566 and HREE depleted in comparison with garnet (Figure 11G). However, as seen in the array plot (Figure
567 11H), the data are displaced from the experimental data, which indicates that zircon and garnet were
568 not in equilibrium. In this case, garnet might have crystallized earlier than zircon, since it shows an
569 enriched pattern in HREE (Figure 4), while zircon shows a flat HREE pattern (Figure 9). HREE are

570 strongly partitioned into garnet (Chen et al., 2010), thus garnet had already sequestered HREE when
571 the zircon rims and soccer balls crystallized.

572 The isobaric-cooling path earlier discussed shows that the garnet modal proportion increases as
573 melt crystallizes toward low temperature, as predicted in the pseudosection modelling (Figure 5). It is
574 likely that the age recorded by the low U zircon group from VAB01 and VAB19, at *ca.* 600-595 Ma,
575 represents the age of crystallization of late trapped melt. It is worth highlighting that two SHRIMP spot
576 analyses from sample RGM55 yielded similar dates (concordia age of 597.3 ± 5.1 Ma) and although they
577 have low statistical representation, these two points might represent the end of leucosome
578 crystallization. Therefore, with the onset of melt crystallization at *ca.* 615 Ma, the duration of melt
579 crystallization is inferred to last for *ca.* 20 Myr (Figure 10).

580 **5.3 Regional implications**

581 **5.3.1 The Guaxupé Domain**

582 Calculated *P–T* conditions using phase equilibrium modelling and conventional
583 thermobarometry demonstrate that all three studied samples, which are located 30 kilometers apart,
584 reached UHT conditions during metamorphism. Similarly high metamorphic conditions have been
585 reported from other rocks associated with the Socorro-Guaxupé Nappe (*e.g.* Del Lama et al., 2000; Rocha
586 et al., 2017). Extreme temperatures are consistent with extensive charnockite magmatism in the area
587 (Janasi, 2002; Salazar-Mora et al., 2014). In summary, we propose that UHT conditions were widespread
588 within the orogen, although mineral associations diagnostic of UHT metamorphism have never been
589 recognized.

590 The Guaxupé Domain is composed of different protoliths, including pelites, and mafic and felsic
591 igneous rocks, with felsic igneous rocks being the most voluminous. Inferred magmatic crystallization
592 ages appear to be only slightly older than the metamorphic event (Campos Neto & Caby, 2000; Campos
593 Neto et al., 1996; Salazar-Mora et al., 2014; Rocha et al., 2017; Rocha, 2016; Tedeschi, 2018). On the one
594 hand, the $^{176}Hf/^{177}Hf$ ratios show a horizontal spreading related to crystallization ages of the zircon
595 grains of all samples (Figure 9F), suggesting that the U-Pb isotopic system were opened during the UHT

event, while the Lu-Hf remained closed. On the other hand, zircon cores are roughly clustered at lower $^{176}Hf/^{177}Hf$ ratios values than the metamorphic domains, particularly in VAB19, which also suggest a slight enrichment in radiogenic ^{176}Hf. Newly formed zircon domains are prone to incorporate radiogenic ^{176}Hf (Gerdes and Zeh, 2009), however, due to the limited time interval between the magmatism and the metamorphic event, significant enrichment was not expected. It is crucial to say that recently zircons of Neoarchean to Paleoproterozoic age have been dated in both the residue and leucosome in rocks located ~70km to the west of the study area (Tedeschi et al., 2018), the first record of such ancient ages in this region.

In this work, the cores of analyzed zircon crystals from garnet-bearing felsic granulite (VAB01 and VAB19) have ages between 705 and 630 Ma and REE patterns characterized by relative enrichment in LREE and strong enrichment in HREE, which generally is different from patterns of other identified zircon groups, which may represent magmatic ages. Zircon crystals from the diatexite (RGM55) also show older ages scattered between 660 and 630 Ma that may be magmatic, although the REE patterns and Hf signatures of these grains are different from those within the felsic garnet granulite. These dates suggest a protracted magmatic event, lasting some 75 Myr, although they could also indicate variable Pb loss along the concordia from a single older magmatic population during UHT metamorphism. Many authors have advocated that these zircon cores are related to the generation of a pre-collisional magmatic arc (*e.g.* Campos Neto et al., 1996; Campos Neto and Caby, 2000; Salazar-Mora et al., 2014). However, in this study, the Hf signatures of zircon cores suggest a crustal source for the magmas. Importantly, there are no juvenile signatures (as observed in Figure 9D), suggesting these rocks represent reworked older continental crust, as indicated by the negative $\varepsilon Hf_{(t)}$ and εNd values (Janasi, 2002; Rocha et al., 2018; Salazar-Mora et al., 2014; Tedeschi et al., 2018) and the newly found Neoarchean-Paleoproterozoic ages (Tedeschi et al., 2018).

5.3.2 The Brasília Orogeny

The granulites of the Guaxupé Domain in this study show a metamorphic peak at around 1000°C and 11.5 kbar, which implies a high T/P ratio (around 870°C GPa^{-1}). Although there are only limited

thermobarometric data published for this domain, similar conditions have been described here before (Del Lama et al., 2000; Garcia and Campos Neto, 2003; Rocha et al., 2018, 2017). A compilation of these data yields an average of T/P ratio of 818°C GPa^{-1} (Figure 12).

On the other hand, the central domain of the southmost part of the Brasília Orogen, the Andrelândia Nappe System, has more detailed data on the metamorphic peak conditions (Campos Neto et al., 2010; Cioffi et al., 2012; Garcia and Campos Neto, 2003; Motta et al., 2010; Motta and Moraes, 2017; Santos et al., 2004). This portion shows a greater diversity of metamorphic grade, from low amphibolite facies to high-pressure granulite (*e.g.* Motta and Moraes, 2017). The T/P ratio in this domain shows lower values than the Guaxupé Domain, with an average of 596°C GPa^{-1} (Figure 12).

Thus, the southmost part of Brasília Orogen shows a bimodal distribution of metamorphism, as observed in the histogram (Figure 12), with two distinct populations. This dualism in the metamorphic conditions is consistent with the evolution of plate tectonics through time (Brown and Johnson, 2018; Holder et al., 2019). However, the low T/P group is at least 100°C GPa^{-1} higher when compared to the Phanerozoic orogens, which show T/P ratios <500°C GPa^{-1} (Holder et al., 2019). Actually, these values are even higher than those predicted for low T/P rocks in Neoproterozoic orogens (Holder et al., 2019) (Figure 12), showing that the conditions of heating were anomalous in this region during the closure of West Gondwana. Nevertheless, the data seem to confirm the idea of gradual changes in the style of plate tectonics and the progressive decreasing of mantle temperatures through time.

6 CONCLUSIONS

The present study has demonstrated that:

- The Guaxupé Domain in the southernmost part of the Brasília Orogen underwent widespread regional UHT metamorphism with peak conditions ranging from 900 to 1050°C at 9 to 12 kbar;
- Modified textures in zircon crystal cores, such as ghost oscillatory zoning and disturbed patterns may represent the recrystallization of magmatic zircon at peak conditions (*ca.* 625 Ma);

- High-U zircon grains and rims record ages of *ca.* 615 Ma, which represent Zr saturation in the melt, close to the onset of melt crystallization;
- A final period of melt crystallization occurred at 870°C at 8.5 kbar in a field where garnet was crystallizing and is marked by *ca.* 595 Ma soccer ball zircon crystals and rims depleted in U and HREE in the garnet-bearing felsic granulite;
- This evolution defines a clockwise *P–T* path suggesting that the lower crust was heated to high-grade conditions for at least 30 Myr (625 to 595 Ma) and that the crystallization of partial melt lasted 20 Myr (615 to 595 Ma);
- A *T/P* comparison with the Andrelândia Nappe System shows a bimodal metamorphic distribution, consistent with the evolution of plate tectonics through time.

ACKNOWLEDGEMENTS

This research was supported by FAPESP (grant 13/04007-0 and 16/22627-3) and Australian Research Council Discovery Project (grant DP150102773). R.G. Motta acknowledges his CNPq (142032/2014-0) and FAPESP scholarships (15/22355-0 and 16/10276-1). The authors acknowledge the use of Curtin University's Microscopy & Microanalysis Facility, GeoHistory Facility and SHRIMP Facility, especially to Elaine Miller, Brad MacDonald and Dr. Cristina Talavera, whose instrumentation has been partially funded by the University, State and Commonwealth Governments. Marcos Mansueto, from the Microprobe Laboratory of Geosciences Institute (University of São Paulo), Dr. Daniel Godoy and Prof. G.L. Luvizotto from Electron Microprobe Laboratory of Universidade Estadual Paulista (UNESP) were also helpful during data collection.

REFERENCES

Baldwin, J.A., Powell, R., Brown, M., Moraes, R., Fuck, R.A., 2005. Modelling of mineral equilibria in ultrahigh-temperature metamorphic rocks from the Anápolis-Itauçu Complex, central Brazil. J. Metamorph. Geol. 23, 511–531. https://doi.org/10.1111/j.1525-1314.2005.00591.x

Braga, I.F., 2002. Análise de deformação de rochas infracrustais da região de Cristina e Itajubá - MG. Universidade Estadual Paulista.

Brito Neves, B.B., Campos Neto, M.C., Fuck, R.A., 1999. From Rodinia to Western Gondwana: An approach

674 to the Brasiliano-Pan African Cycle and orogenic collage. Episodes 22, 155–166.
675 https://doi.org/10.18814/epiiugs/1999/v22i3/002

676 Brito Neves, B.B., Fuck, R.A., 2013. Neoproterozoic evolution of the basement of the South-American
677 platform. J. South Am. Earth Sci. 47, 72–89. https://doi.org/10.1016/j.jsames.2013.04.005

678 Brown, M., 2007. Metamorphism, Plate Tectonics, and the Supercontinent Cycle. Earth Sci. Front. 14, 1–
679 18. https://doi.org/10.1016/S1872-5791(07)60001-3

680 Brown, M., Johnson, T., 2018. Secular change in metamorphism and the onset of global plate tectonics.
681 Am. Mineral. 103, 181–196. https://doi.org/10.2138/am-2018-6166

682 Campos Neto, M.C., 2000. Orogenetic systems from Southwestern Gondwana: an approach to Brasiliano-
683 Pan African cycle and orogenic collage in southeastern Brazil, in: Cordani, U.G., Milani, E.J., Thomaz
684 Filho, A., Campos, D.A. (Eds.), Tectonic Evolution of South America. Rio de Janeiro, pp. 335–365.

685 Campos Neto, M.C., Basei, M.A.S., Vlach, S.R.F., Caby, R., Szabó, G.J.A., Vasconcelos, P., 2004. Migração de
686 orógenos e superposição de orogêneses: um esboço da Colagem Brasiliana no sul do Cráton São
687 Francisco, SE - Brasil. Geol. USP - Série científica 4, 13–40.

688 Campos Neto, M.C., Caby, R., 2000. Terrane accretion and upward extrusion of high-pressure granulites
689 in the Neoproterozoic nappes of southeast Brazil: Petrologic and structural constraints. Tectonics
690 19, 669–687. https://doi.org/10.1029/1999TC900065

691 Campos Neto, M.C., Caby, R., 1999. Neoproterozoic high-pressure metamorphism and tectonic
692 constraint from the nappe system south of the São Francisco Craton, southeast Brazil. Precambrian
693 Res. 97, 3–26. https://doi.org/10.1016/S0301-9268(99)00010-8

694 Campos Neto, M.C., Cioffi, C.R., Moraes, R., Motta, R.G., Siga Jr., O., Basei, M.A.S., 2010. Structural and
695 metamorphic control on the exhumation of high-P granulites: The Carvalhos Klippe example, from
696 the oriental Andrelândia Nappe System, southern portion of the Brasília Orogen, Brazil.
697 Precambrian Res. 180, 125–142. https://doi.org/10.1016/j.precamres.2010.05.010

698 Campos Neto, M.C., Janasi, V. de A., Caby, R., 1996. Ocorrência de granulitos empobrecidos nas porções

699 basais da nappe de empurrão Socorro-Guaxupé. Bol. IG-USP 18, 11–13.

700 Chen, R.-X., Zheng, Y.-F., Xie, L., 2010. Metamorphic growth and recrystallization of zircon: Distinction
701 by simultaneous in-situ analyses of trace elements, U–Th–Pb and Lu–Hf isotopes in zircons from
702 eclogite-facies rocks in the Sulu orogen. LITHOS 114, 132–154.
703 https://doi.org/10.1016/j.lithos.2009.08.006

704 Cioffi, C. R., Campos Neto, M. da C., Möller, A., Rocha, B.C., 2016a. Tectonic significance of the Meso- to
705 Neoarchean complexes in the basement of the southern Brasília Orogen. Precambrian Res. 287,
706 91–107. https://doi.org/10.1016/j.precamres.2016.10.009

707 Cioffi, C.R., Campos Neto, M.C., Moller, A., Rocha, B.C., 2016b. Paleoproterozoic continental crust
708 generation events at 2.15 and 2.08 Ga in the basement of the southern Brasília Orogen, SE Brazil.
709 Precambrian Res. 275, 176–196. https://doi.org/10.1017/CBO9781107415324.004

710 Cioffi, C.R., Campos Neto, M.C., Rocha, B.C., Moraes, R., Henrique-Pinto, R., 2012. Geochemical signatures
711 of metasedimentary rocks of high-pressure granulite facies and their relation with partial melting:
712 Carvalhos Klippe, Southern Brasília Belt, Brazil. J. South Am. Earth Sci. 40, 63–76.
713 https://doi.org/10.1016/j.jsames.2012.09.007

714 Clark, C., Fitzsimons, I.C.W., Healy, D., Harley, S.L., 2011. How Does the Continental Crust Get Really Hot?
715 Elements 7, 235–240. https://doi.org/10.2113/gselements.7.4.235

716 Coelho, M.B., Trouw, R.A.J., Ganade, C.E., Vinagre, R., Mendes, J.C., Sato, K., 2017. Constraining timing and
717 P-T conditions of continental collision and late overprinting in the Southern Brasília Orogen (SE-
718 Brazil): U-Pb zircon ages and geothermobarometry of the Andrelândia Nappe System. Precambrian
719 Res. 292, 194–215. https://doi.org/10.1016/j.precamres.2017.02.001

720 de Laeter, J.R., Kennedy, A.K., 1998. A double focusing mass spectrometer for geochronology. Int. J. Mass
721 Spectrom. 178, 43–50. https://doi.org/10.1016/S1387-3806(98)14092-7

722 Del Lama, E.A., Oliveira, M.A.F., Zanardo, A., 1998. Geochemistry of the Guaxupé Granulites, Minas Gerais,
723 Brazil. Gondwana Res. 1, 357–365. https://doi.org/10.1016/S1342-937X(05)70851-0

724 Del Lama, E.A., Oliveira, M.A.F., Zanardo, A., 1994. Geotermobarometria em rochas do Complexo Campos
725 Gerais ao norte da Zona de Cisalhamento Varginha. Rev. Bras. Geociências 24, 233–239.

726 Del Lama, E.A., Zanardo, A., Oliveira, M.A.F., Morales, N., 2000. Exhumation of high-pressure granulites
727 of the Guaxupé Complex, southeastern Brazil. Geol. J. 35, 231–249. https://doi.org/10.1002/gj.859

728 Evans, K.A., 2012. The redox budget of subduction zones. Earth-Science Rev. 113, 11–32.
729 https://doi.org/10.1016/j.earscirev.2012.03.003

730 Fetter, A.H., Hackspacher, P.C., Ebbert, H.D., Dantas, E.L., Costa, A.C.D., 2001. New Sm/Nd and U/Pb
731 geochronological constraints of the Archean to neoproterozoic evolution of the Amparo basement
732 complex of the Central Ribeira Belt, Southeastern Brazil, in: South American Symposium on Isotope
733 Geology. Sociedad Geológica de Chile, Pucon, Chile.

734 Fitzsimons, I.C.W., Harley, S.L., 1994. The Influence of Retrograde Cation Exchange on Granulite P-T
735 Estimates and a Convergence Technique for the Recovery of Peak Metamorphic Conditions. J.
736 Petrol. 35, 543–576. https://doi.org/10.1093/petrology/35.2.543

737 Frugis, G.L., Campos Neto, M. da C., Lima, R.B., 2018. Eastern Paranapanema and southern São Francisco
738 orogenic margins: Records of enduring Neoproterozoic oceanic convergence and collision in the
739 southern Brasília Orogen. Precambrian Res. 308, 35–57.
740 https://doi.org/10.1016/j.precamres.2018.02.005

741 Garcia, M.G.M., Campos Neto, M.C., 2003. Contrasting metamorphic conditions in the Neoproterozoic
742 collision-related Nappes south of São Francisco Craton , SE Brazil. J. South Am. Earth Sci. 15, 853–
743 870. https://doi.org/10.1016/S0895-9811(02)00147-5

744 Genco, R.M., 2014. Petrologia de ortognaisses e granitóides do Domínio Socorro, Nappe Socorro-
745 Guaxupé, Seção Extrema-Camanducaia. Universidade de São Paulo.
746 https://doi.org/10.11606/D.44.2014.tde-03122014-095629

747 Gerdes, A., Zeh, A., 2009. Zircon formation versus zircon alteration — New insights from combined U–
748 Pb and Lu–Hf in-situ LA-ICP-MS analyses, and consequences for the interpretation of Archean

749 zircon from the Central Zone of the Limpopo Belt. Chem. Geol. 261, 230–243.
750 https://doi.org/10.1016/j.chemgeo.2008.03.005

751 Green, E.C.R., White, R.W., Diener, J.F.A., Powell, R., Holland, T.J.B., Palin, R.M., 2016. Activity–composition
752 relations for the calculation of partial melting equilibria for metabasic rocks. J. Metamorph. Geol.
753 34, 845–869. https://doi.org/10.1017/CBO9781107415324.004

754 Grimes, C.B., Wooden, J.L., Cheadle, M.J., John, B.E., 2015. "Fingerprinting" tectono-magmatic provenance
755 using trace elements in igneous zircon. Contrib. to Mineral. Petrol. 170, 46.
756 https://doi.org/10.1007/s00410-015-1199-3

757 Harley, S.L., 2008. Refining the P-T records of UHT crustal metamorphism. J. Metamorph. Geol. 26, 125–
758 154. https://doi.org/10.1111/j.1525-1314.2008.00765.x

759 Harley, S.L., 1998. On the occurrence and characterization of ultrahigh-temperature crustal
760 metamorphism, in: Treoloar, P.J., O'Brien, P.J. (Eds.), What Drives Metamorphism and Metamorphic
761 Reactions? Geological Society, London, Special Publications, Londres, pp. 81–107.
762 https://doi.org/10.1144/GSL.SP.1996.138.01.06

763 Hermann, J., 2002. Allanite: thorium and light rare earth element carrier in subducted crust. Chem. Geol.
764 192, 289–306. https://doi.org/10.1016/S0009-2541(02)00222-X

765 Holder, R.M., Viete, D.R., Brown, M., Johnson, T.E., 2019. Metamorphism and the evolution of plate
766 tectonics. Nature 572, 378–381. https://doi.org/10.1038/s41586-019-1462-2

767 Holland, T., Powell, R., 2001. Calculation of phase relations involving haplogranitic melts using an
768 internally consistent thermodynamic dataset. J. Petrol. 42, 673–683.
769 https://doi.org/10.1093/petrology/42.4.673

770 Holland, T.J.B., Powell, R., 2003. Activity-compositions relations for phases in petrological calculations:
771 An asymetric multicomponent formulation. Contrib. to Mineral. Petrol. 145, 492–501.
772 https://doi.org/10.1007/s00410-003-0464-z

773 Holland, T.J.B., Powell, R., 1998. An internally consistent thermodynamic data set for phases of

774 petrological interest. J. Metamorph. Geol. 16, 309–343. https://doi.org/10.1111/j.1525-
775 1314.1998.00140.x

776 Holness, M.B., Cesare, B., Sawyer, E.W., 2011. Melted Rocks under the Microscope: Microstructures and
777 Their Interpretation. Elements 7, 247–252. https://doi.org/10.2113/gselements.7.4.247

778 Iyer, S.S., Choudhuri, A., Pattison, D.R.M., De Paoli, G.R., 1996. Petrology and geochemistry of the
779 Neoproterozoic Guaxupé granulite facies terrain, southeastern Brazil. Precambrian Res. 77, 23–40.
780 https://doi.org/10.1016/0301-9268(95)00043-7

781 Jackson, S.E., Pearson, N.J., Griffin, W.L., Belousova, E.A., 2004. The application of laser ablation-
782 inductively coupled plasma-mass spectrometry to in situ U–Pb zircon geochronology. Chem. Geol.
783 211, 47–69. https://doi.org/10.1016/j.chemgeo.2004.06.017

784 Janasi, V.A., 2002. Elemental and Sr-Nd isotope geochemistry of two Neoproterozoic mangerite suites in
785 SE Brazil: implications for the origin of the mangerite-charnockite-granite series. Precambrian Res.
786 119, 301–327. https://doi.org/10.1016/S0301-9268(02)00127-4

787 Janasi, V.A., 1999. Petrogênese de granitos crustais na Nappe de Empurrão Socorro-Guaxupé (SP-MG):
788 uma contribuição da geoquímica elemental e isotópica. Universidade de São Paulo.

789 Kelsey, D.E., 2008. On ultrahigh-temperature crustal metamorphism. Gondwana Res. 13, 1–29.
790 https://doi.org/10.1016/j.gr.2007.06.001

791 Kelsey, D.E., Hand, M., 2015. On ultrahigh temperature crustal metamorphism: Phase equilibria, trace
792 element thermometry, bulk composition, heat sources, timescales and tectonic settings. Geosci.
793 Front. 6, 311–356. https://doi.org/10.1016/j.gsf.2014.09.006

794 Kennedy, A.K., de Laeter, J.R., 1994. The performance characteristics of the WA SHRIMP II ion
795 microprobe. US Geol. Surv. Circ. 1107, 16.

796 Kohn, M.J., Penniston-Dorland, S.C., 2017. Diffusion: Obstacles and Opportunities in Petrochronology.
797 Rev. Mineral. Geochemistry 83, 103–152. https://doi.org/10.2138/rmg.2017.83.4

798 Korhonen, F.J., Clark, C., Brown, M., Taylor, R.J.M., 2014. Taking the temperature of Earth's hottest crust.

799 Earth Planet. Sci. Lett. 408, 341–354. https://doi.org/10.1016/j.epsl.2014.10.028

800 Ludwig, K., 2009. SQUID II User's Manual, Berkeley Geochronological Center Special Publication.

801 Ludwig, K.R., 2003. Isoplot/Ex 3.00: A geochronological toolkit for Microsoft Excel, 4th ed, Berkeley
802 Geochronology Centre.

803 Martins, L., Vlach, S.R.F., Janasi, V.D.A., 2009. Reaction microtextures of monazite: Correlation between
804 chemical and age domains in the Nazaré Paulista migmatite, SE Brazil. Chem. Geol. 261, 271–285.
805 https://doi.org/10.1016/j.chemgeo.2008.09.020

806 Middlemost, E.A.K., 1994. Naming materials in the magma/igneous rock system. Earth-Science Rev. 37,
807 215–224. https://doi.org/10.1016/0012-8252(94)90029-9

808 Moraes, R., Benetti, B.Y., Motta, R.G., 2015. Ultrahigh-temperature metamorphism in granulites with "no
809 classic" mineral assemblage, in: 8th Hutton Symposium on Granites and Related Rocks.
810 Florianópolis, Brazil.

811 Moraes, R., Brown, M., Fuck, R.A., Camargo, M.A., Lima, T.M., 2002. Characterization and P–T Evolution
812 of Melt- bearing Ultrahigh-temperature Granulites: an Example from the Anápolis-Itauçu Complex
813 of the Brasília Fold Belt Brazil. J. Petrol. 43, 1673–1705.
814 https://doi.org/10.1093/petrology/43.9.1673

815 Mori, P.E., Reeves, S., Correia, C.T., Haukka, M., 1999. Development of a fused glass disc XRF facility and
816 comparison with the pressed powder pellet technique at Instituto de Geociencias, Sao Paulo
817 University. Rev. Bras. Geociencias 29, 441–446.

818 Motta, R.G., Moraes, R., 2017. Pseudo- and real-inverted metamorphism caused by the superposition and
819 extrusion of a stack of nappes: a case study of the Southern Brasília Orogen, Brazil. Int. J. Earth Sci.
820 106, 2407–2427. https://doi.org/10.1007/s00531-016-1436-7

821 Motta, R.G., Moraes, R., Trouw, R.A.J., Campos Neto, M.C., 2010. Reconstrução e comparação de
822 trajetórias P-T no Sistema de Nappes Andrelândia, Sul da Faixa Brasília, MG. Geol. USP - Série
823 científica 10, 79–96. https://doi.org/10.5327/Z1519-874X2010000300006

824 Navarro, M.S., Andrade, S., Ulbrich, H., Gomes, C.B., Girardi, V.A. V, 2008. The Direct Determination of
825 Rare Earth Elements in Basaltic and Related Rocks using ICP-MS: Testing the Efficiency of
826 Microwave Oven Sample Decomposition Procedures. Geostand. Geoanalytical Res. 32, 167–180.
827 https://doi.org/10.1111/j.1751-908X.2008.00840.x

828 Paton, C., Hellstrom, J., Paul, B., Woodhead, J., Hergt, J., 2011. Iolite: Freeware for the visualisation and
829 processing of mass spectrometric data. J. Anal. At. Spectrom. 26, 2508–2518.
830 https://doi.org/10.1039/C1JA10172B

831 Pattison, D.R.M., Bégin, N.J., 1994. Zoning patterns in orthopyroxene and garnet in granulites:
832 implications for geothermometry. J. Metamorph. Geol. 12, 387–410.
833 https://doi.org/10.1111/j.1525-1314.1994.tb00031.x

834 Pattison, D.R.M., Chacko, T., Farquhar, J., McFarlane, C.R.M., 2003. Temperatures of granulite-facies
835 metamorphism: constraints from experimental phase equilibria and thermobarometry corrected
836 for retrograde exchange. J. Petrol. 44, 867–900. https://doi.org/10.1093/petrology/44.5.867

837 Powell, R., Holland, T.J.B., 1988. An internally consistent dataset with uncertainties and correlations: 3.
838 Applications to geobarometry, worked examples and a computer program. J. Metamorph. Geol. 6,
839 173–204. https://doi.org/10.1111/j.1525-1314.1988.tb00415.x

840 Reno, B.L., Brown, M., Kobayashi, K., Nakamura, E., Piccoli, P.M., Trouw, R.A.J., 2009. Eclogite – high-
841 pressure granulite metamorphism records early collision in West Gondwana: new data from the
842 Southern Brasília Belt, Brazil. J. Geol. Soc. London. 166, 1013–1032.
843 https://doi.org/10.1144/0016-76492008-140

844 Rocha, B.C., 2016. Idade, duração e condições P-T do metamorfismo de temperatura ultra-alta, anatexia
845 e cristalização de fundido na Nappe Socorro-Guaxupé. Universidade de São Paulo.
846 https://doi.org/10.11606/T.44.2016.tde-28092016-143315

847 Rocha, B.C., Moraes, R., Moller, A., Cioffi, C.R., 2018. Magmatic inheritance vs. UHT metamorphism: zircon
848 petrochronology of granulites and petrogenesis of charnockitic leucossomes of Socorro-Guaxupé
849 Nappe, SE Brazil. Lithos. https://doi.org/10.1016/j.lithos.2018.05.014

Rocha, B.C., Moraes, R., Möller, A., Cioffi, C.R., Jercinovic, M.J., 2017. Timing of anatexis and melt crystallization in the Socorro-Guaxupé Nappe, SE Brazil: insights from trace element composition of zircon, monazite and garnet coupled to U-Pb geochronology. Lithos 277, 337–355. https://doi.org/10.1016/j.lithos.2016.05.020

Salazar-Mora, C., Campos Neto, M.C., Basei, M.A.S., 2014. Syn-collisional lower continental crust anatexis in the Neoproterozoic Socorro-Guaxupé Nappe System, southern Brasília Orogen, Brazil: Constraints from zircon U-Pb dating, Sr-Nd-Hf signatures and whole-rock geochemistry. Precambrian Res. 255, 847–864. https://doi.org/10.1016/j.precamres.2014.10.017

Santos, L.P., Campos Neto, M.C., Grohmann, C.H., 2004. Metamorphic path constrained by metapelitic rocks from the inner Aiuruoca-Andrelândia nappe, south of the São Francisco craton, SE Brazil. J. South Am. Earth Sci. 16, 725–741. https://doi.org/10.1016/j.jsames.2003.12.006

Sláma, J., Košler, J., Condon, D.J., Crowley, J.L., Gerdes, A., Hanchar, J.M., Horstwood, M.S.A., Morris, G.A., Nasdala, L., Norberg, N., Schaltegger, U., Schoene, B., Tubrett, M.N., Whitehouse, M.J., 2008. Plešovice zircon - A new natural reference material for U-Pb and Hf isotopic microanalysis. Chem. Geol. 249, 1–35. https://doi.org/10.1016/j.chemgeo.2007.11.005

Stacey, J.S., Kramers, J.D., 1975. Approximation of terrestrial lead isotope evolution by a two-stage model. Earth Planet. Sci. Lett. 26, 207–221. https://doi.org/10.1016/0012-821X(75)90088-6

Stern, R.A., Bodorkos, S., Kamo, S.L., Hickman, A.H., Corfu, F., 2009. Measurement of SIMS instrumental mass fractionation of Pb isotopes during Zircon dating. Geostand. Geoanalytical Res. 33, 145–168. https://doi.org/10.1111/j.1751-908X.2009.00023.x

Taylor, R.J.M., Clark, C., Harley, S.L., Kylander-Clark, A.R.C., Hacker, B.R., Kinny, P.D., 2017. Interpreting granulite facies events through rare earth element partitioning arrays. J. Metamorph. Geol. 35, 759–775. https://doi.org/10.1111/jmg.12254

Taylor, R.J.M., Kirkland, C.L., Clark, C., 2016. Accessories after the facts: Constraining the timing, duration and conditions of high-temperature metamorphic processes. Lithos 264, 239–257. https://doi.org/10.1016/j.lithos.2016.09.004

876 Tedeschi, M., 2018. Geodynamic evolution of the Southern Brasília orogen (SE Brazil): New
877 petrochronological insights from UHT and HP metamorphic rocks. Universidade Federal de Minas
878 Gerais.

879 Tedeschi, M., Pedrosa-Soares, A., Dussin, I., Lanari, P., Novo, T., Pinheiro, M.A.P., Lana, C., Peters, D., 2018.
880 Protracted zircon geochronological record of UHT garnet-free granulites in the Southern Brasília
881 orogen (SE Brazil): petrochronological constraints on magmatism and metamorphism.
882 Precambrian Res. https://doi.org/10.1016/j.precamres.2018.07.023

883 Trouw, R.A.J., Ribeiro, A., Paciullo, F.V.P., Heilbron, M., 2000. Interference between the Neoproterozoic
884 Brasilia and Ribeira Belts, with special emphasis on high-pressure granulites, in: International
885 Geological Congress. Rio de Janeiro, p. 45p.

886 Vielzeuf, D., Clemens, J.D., Pin, C., Moinet, E., 1990. Granites, Granulites, and Crustal Differentiation, in:
887 Vielzeuf, D., Vidal, P. (Eds.), Granulites and Crustal Evolution. Springer Netherlands, Dordrecht, pp.
888 59–85. https://doi.org/10.1007/978-94-009-2055-2_5

889 Waters, D.J., 2001. The significance of prograde and retrograde quartz-bearing intergrowth
890 microstructures in partially melted granulite-facies rocks. Lithos 56, 97–110.
891 https://doi.org/10.1016/S0024-4937(00)00061-X

892 Wedepohl, K.H., 1995. The composition of the continental crust. Geochim. Cosmochim. Acta 59, 1217–
893 1232. https://doi.org/10.1016/0016-7037(95)00038-2

894 White, R.W., Powell, R., 2002. Melt loss and the preservation of granulite facies mineral assemblages. J.
895 Metamorph. Geol. 20, 621–632. https://doi.org/10.1046/j.1525-1314.2002.00206.x

896 White, R.W., Powell, R., Clarke, G.L., 2002. The interpretation of reaction textures in Fe-rich metapelitic
897 granulites of the Musgrave Block, Central Australia: Constraints from mineral equilibria
898 calculations in the system K2O-FeO-MgO-Al2O3-SiO2-H2O-TiO2-Fe2O3. J. Metamorph. Geol. 20,
899 41–55. https://doi.org/10.1046/j.0263-4929.2001.00349.x

900 White, R.W., Powell, R., Holland, T.J.B., 2007. Progress relating to calculation of partial melting equilibria

for metapelites. J. Metamorph. Geol. 25, 511–527. https://doi.org/10.1111/j.1525-1314.2007.00711.x

White, R. W., Powell, R., Holland, T.J.B., Johnson, T.E., Green, E.C.R., 2014a. New mineral activity-composition relations for thermodynamic calculations in metapelitic systems. J. Metamorph. Geol. 32, 261–286. https://doi.org/10.1111/jmg.12071

White, R W, Powell, R., Johnson, T.E., 2014b. The effect of Mn on mineral stability in metapelites revisited: new a–x relations for manganese-bearing minerals. J. Metamorph. Geol. 32, 809–828. https://doi.org/10.1111/jmg.12095

Yakymchuk, C., Kirkland, C.L., Clark, C., 2018. Th/U ratios in metamorphic zircon. J. Metamorph. Geol. https://doi.org/10.1111/jmg.12307

List of Supporting Information

Figure S1. *T*–X pseudosection (sample VAB01 – garnet-bearing felsic granulite), where X varies from 0.01 to 5 mol. % of H_2O. Dashed lines are the modal proportions of melt. It was chosen a value (red dashed line) to cover among 5 and 20% of melt at the assemblage peak (aug-opx-g-ilm-ksp-L)

Figure S2. *P*–X pseudosection, where XFe_2O_3 varies from 0.2 to 1.75 mol. %. An XFe_2O_3 value of 0.98 mol. % was chosen (blue dashed line) to eliminate rutile from the calculations.

Figure S3. Comparison between $^{206}Pb/^{238}U$ age obtained by SHRIMP and LASS–ICP–MS. (A) All the data, where blue balls are sample VAB01, yellow triangles are sample VAB19 and red diamonds are sample RGM55; (B) Sample VAB01; (C) Sample VAB19; and (D) Sample RGM55. In (B), (C) and (D) uncertainties bars are given in 2σ. Note that LASS–ICP–MS tends to yield older ages than SHRIMP.

Figure S4. Pseudosections (VAB19). (A) *T*–X, where X varies from 0.01 to 4.74 mol. % of H_2O. Dashed lines are the modal proportions of melt. It was chosen a value (red line) to cover among 5 and 20% of melt at the assemblage peak (aug-opx-g-ilm-ksp-L). (B) *P*–X, where XFe_2O_3 varies from 0.2 to 1.75 mol. %. An XFe_2O_3 value of 0.98 mol. % was chosen (red line) to eliminate rutile from the calculations. (C) *P*–

925 *T*, contours show the modal proportion of melt (dashed lines), and the solidus is represented by a bold
926 red line. The peak mineral association is highlighted in yellow.

927 Table S1. Representative EMP data of silicates.

928 Table S2. Representative LA–ICP–MS data of garnet.

929 Table S3. Chemical analyses of granulites.

930 Table S4. SHRIMP U–Pb data of zircon.

931 Table S5. LASS–ICP–MS complementary U–Pb data of zircon

932 Table S6. LASS–ICP–MS trace elements data of zircon.

933 Table S7. LASS–ICP–MS Lu–Hf data of zircon.

934 **Figure Captions**

935 Figure 1. (A) Brasília Orogen and its relation with Neoproterozoic orogens and cratons of eastern Brazil.
936 (B) Geological Map of the Guaxupé Domain of the Socorro-Guaxupé Nappe, Southern Brasília Orogen
937 (after Campos Neto et al., 2010). Numbers 1 to 4 are the location of the studied samples VAB01, VAB19,
938 RGM55 and PAR03, respectively, two garnet-bearing felsic granulites, a diatexite and a garnet mafic
939 granulite. Previous works are labelled: green box is Del Lama et al. (1998); red star is Rocha et al. (2017);
940 yellow star is Rocha et al. (2018); and blue box is Tedeschi et al. (2018).

941 Figure 2. (A) Banded garnet-bearing felsic granulite with orthopyroxene porphyroblast (VAB01). (B)
942 Typical mineral assemblage of the banded garnet-bearing felsic granulite with two pyroxenes in both
943 the residuum and in the leucosome (VAB19, plane-polarized light). (C) Films of quartz (arrows)
944 surrounding feldspars in the garnet-bearing felsic granulite, representing evidence of former anatectic
945 melt (crossed polarized light plus λ plate – VAB01). (D) Films of K-feldspar wrapping plagioclase crystals
946 in the garnet-bearing felsic granulite (BSE image – VAB19). (E) Rounded biotite inclusions in garnet and
947 hornblende replacing pyroxene outside garnet in the garnet-bearing felsic granulite (VAB01, plane-
948 polarized light). (F) Clinopyroxene (darker grey) in the garnet-bearing felsic granulite with fine
949 exsolution lamellae of clinoenstatite (brighter grey) and an adjacent oxide phase in the top right corner

oxide comprising exsolved ilmenite (brightest grey) and magnetite (VAB01, BSE image). (G) Biotite and oxide intergrowths surrounding pyroxene grains in the diatexite (RGM55, plane-polarized light). (H) Coarse allanite crystals in leucosome of the diatexite (RGM55, plane-polarized light). (I) Fine to coarse-grained garnet mafic granulite with granoblastic fabric (PAR03, plane-polarized light).

Figure 3. (A) TAS diagram (Middlemost, 1994) for the rocks of this work. The green shaded area represent basic granulites, the red area intermediate granulites and yellow area acid granulite. Classification and data follow-Del Lama et al. (1998). (B) Chondrite-normalized (Sun and McDonough, 1989) REE patterns for the garnet-bearing felsic granulites and diatexite; (C) Average continental crust-normalized (Wedepohl, 1995) trace-element patterns for the garnet-bearing felsic granulites and diatexite.

Figure 4. Representative compositional profiles from analytical traverses across garnet grains acquired by EMP (figures A, C and E) and LA–ICP–MS (figures B and D). Sample ID is labelled in the figure. In (B), core 1 represents the centres of those crystals bigger than ~7 mm, and core 2 the intermediate portions of these big grains and centres of smaller grains.

Figure 5. (A) Calculated *P*–*T* pseudosection for the bulk composition of VAB01, a garnet-bearing felsic granulite, using the augite model for clinopyroxene. Contours show the modal proportion of melt (dashed lines), and the solidus is represented by a bold white line. The peak mineral association is highlighted in yellow. Al^{T} isopleths in orthopyroxene marked by magenta lines with their respective values. (B) Calculated changes in modal proportions of phases at 10 kbar for sample VAB01, a garnet-bearing felsic granulite.

Figure 6. Calculated *P*–*T* pseudosection for a garnet-bearing garnet mafic granulite (PAR03), using an augite model for clinopyroxene. The peak mineral association is highlighted in yellow. (A) Water content around 1 mol. %. (B) Water content of 0.01 mol. %. Contours for the modal proportion of melt are shown with dashed lines, and the solidus is represented by a bold white line.

Figure 7. CL images for representative zircon crystals from the three studied samples. Yellow ellipses show the location of SHRIMP spots (~ 20 μm diameter) and blue circles the location of LASS–ICP–MS

spots (~ 50 μm diameter). Labels present spot ID, $^{206}Pb/^{238}U$ date (Ma) with 1σ uncertainties, U content (ppm) and $\varepsilon Hf_{(t)}$ values, when the latter is available. Labels in yellow show SHRIMP data, while labels in blue LASS–ICP–MS data. (A) Sample VAB01, oscillatory-zoned cores show older ages and higher U than soccer ball crystals. (B) Sample VAB19, oscillatory-zoned cores show older ages and higher U than rims and soccer ball crystals. (C) Sample RGM55, broad oscillatory cores show the oldest ages, sector- and disturbed-zoned cores older than rims and soccer ball crystals, and anhedral grain show the youngest age.

Figure 8. Concordia diagrams with zircon U–Pb isotopic data collected with SHRIMP II (2σ error ellipses) in (A), (B), (C) in which: (A) Data for sample VAB01 from soccer ball zircon (sb) and rims with a weighted mean $^{206}Pb/^{238}U$ age of 593.8 ± 8.5 Ma and cores ranging up to *ca.* 700 Ma; (B) Data for sample VAB19 from soccer ball zircon and rims with a weighted mean $^{206}Pb/^{238}U$ age of 598 ± 4.6 Ma and cores ranging up to *ca.* 700 Ma; (C) Data for sample RGM55, where blue ellipses represent the oldest ages, red ellipses are zircon cores with a weighted mean $^{206}Pb/^{238}U$ age of 624.8 ± 3.4 Ma, yellow ellipses are soccer ball and shapeless zircon and rims with a weighted mean $^{206}Pb/^{238}U$ age of 615.8 ± 3.4 Ma, and green ellipses are shapeless zircon with Concordia age of 597.3 ± 5.1 Ma. Contents of Th and U (obtained by SHRIMP, except group 5, which was obtained in LASS–ICP–MS) of different zircon types are shown in (D), in which: 1 – oscillatory-zoned cores from VAB01; 2 – rims and soccer ball crystals from VAB01; 3 – oscillatory-zoned cores from VAB19; 4 – rims and soccer ball crystals from VAB19; 5 – older broad oscillatory-zoned or sector-zoned cores from RGM55; 6 – 625 Ma sector-zoned core from RGM55; 7 – 615 Ma high U domain from RGM55;and 8 – 597 Ma anhedral zircon from RGM55.

Figure 9. Zircon REE chondrite-normalized pattern (Sun and McDonough, 1989) in (A) to (C), in which: (A) VAB01; (B) VAB19; (C) RGM55; (D) $^{176}Hf/^{177}Hf$ against $^{206}Pb/^{238}U$ for different zircon types (LASS–ICP–MS Hf data linked to SHRIMP ages data), in which: 1 – oscillatory-zoned cores from VAB01; 2 – soccer ball crystals from VAB01. 3 – rims from VAB01; 4 – oscillatory-zoned cores from VAB19; 5 – soccer ball crystals from VAB19; 6 – rim from VAB19; 7 – older domain from RGM55; 8 – 625 Ma sector-zoned cores from RGM55; 9 – 615 Ma high-U domains from RGM55; 10 – 597 Ma domain from RGM55. Shaded areas are data from Tedeschi et al. (2018).

1003 Figure 10. Summary of *P*–*T*–t estimates for rocks of the Guaxupé Domain. Peak fields for samples VAB01
1004 (felsic granulite) and PAR03 (mafic granulite) are overlain to show the region of overlap. Calculated in
1005 pseudosection Al^T isopleth in orthopyroxene is at similar conditions to those calculated in the average
1006 *P*–*T* mode of THERMOCAL*CA.* The post-peak evolution leads to the magnetite growth coexisting with
1007 garnet. Crystallization of high U rims and the formation of xenomorphic and soccer ball zircon at *ca* 615
1008 Ma, might be linked with the Zr saturation in the melt in the onset of melt crystallization. The end of the
1009 crystallization of the melt happened at 870°C and 8.5 kbar and it is marked by the crystallization of low
1010 U rims and soccer ball zircon depleted in HREE at *ca.* 595 Ma. The prograde evolution is dashed because
1011 the uncertainties around the protolith, and partial melt and melt segregation mean that the present-day
1012 bulk composition may not be representative of previous conditions, although sector-zoned zircon grains
1013 are representative of this period at *ca.* 625 Ma.

1014 Figure 11. Zircon and garnet trace elements data from garnet-bearing felsic granulite (VAB01 and
1015 VAB19). Traditional DREE (zircon–garnet) plot in (A), (C), (E) and (G). Array plot, purposed by Taylor
1016 et al. (2017), showing DREE (zircon–garnet) for all zircon against average garnet domains in (B), (D),
1017 (F) and (H). (A) and (B) zircon data plotted against garnet cores depleted in HREE from sample VAB01
1018 (core 1 from Figure 4B). (C) and (D) zircon data plotted against cores/intermediate portion of garnet
1019 from sample VAB01 (core 2 from Figure 4B). (E) and (F) zircon data plotted against garnet rims from
1020 sample VAB01 (rim from Figure 4B). (G) and (H) zircon data plotted against the single garnet domain
1021 from sample VAB19 (Figure 4D). (*) zircon–garnet data from Taylor et al. (2015) performed at 7 kbar.
1022 (**) zircon–garnet data from Rubatto and Hermann (2007) performed at 20 kbar.

1023 Figure 12. (A) Distribution of *T/P* ratios in the southmost part of Brasília Orogen showing two
1024 populations, one of high *T/P*, represented by the Guaxupé Domain (n=8) and other of low *T/P*,
1025 represented by the Andrelândia Nappe System (n=14). The pink box represents the expected low *T/P*
1026 group for a Neoproterozoic age of 625 Ma, whereas the blue box is what were expected for the high *T/P*
1027 group, according with Holder et al. (2019). (B) *P*–*T* conditions of metamorphic peak in the southmost
1028 part of Brasília Orogen. In both figures, blue symbols are data from Guaxupé Domain and red symbol
1029 are data from Andrelândia Nappe System; references are labelled inside the figure.

Table Captions

Table 1. Bulk composition as molar oxides (mol.%) used in phase equilibria modelling.

Table 2. Summary of conventional thermobarometric results. The uncertainties of THERMOCALC are reported as 2σ.

Figure 1

Click here to access/download;Figure;Fig 1.tif

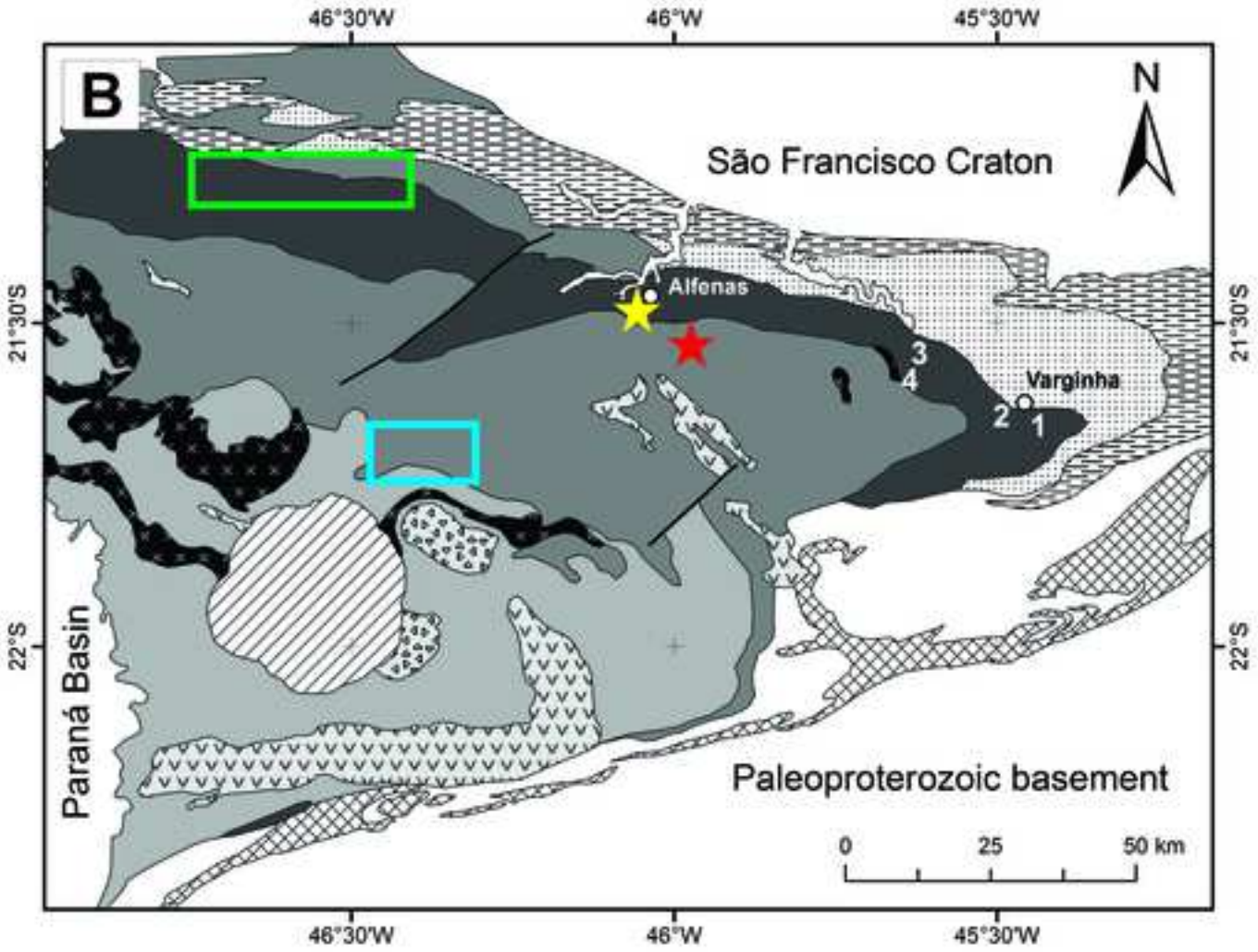

Cretaceous

- Poços de Caldas Alkaline Massif

Neproterozoic (Andrelândia Nappe System)

- Três Pontas-Varginha Nappe
- Liberdade Nappe
- Carmo da Cachoeira Nappe

Neoproterozoic (Socorro-Guaxupé Nappe)

- Late and Post-orogenetic granites
- Syn-orogenetic granites
- Granulitic Unit
- Diatexitic Unit
- Metatexitic Unit
- Charnockite Suite
- Del Lama et al. (1998)
- Rocha et al. (2017)
- Rocha et al. (2018)
- Tedeschi et al. (2018)

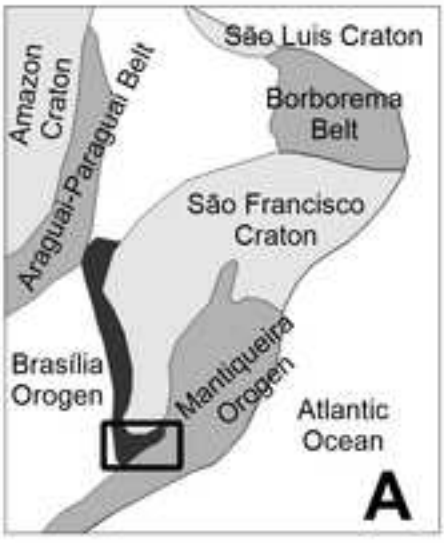

Figure 2

Click here to access/download;Figure;Fig 2.tif

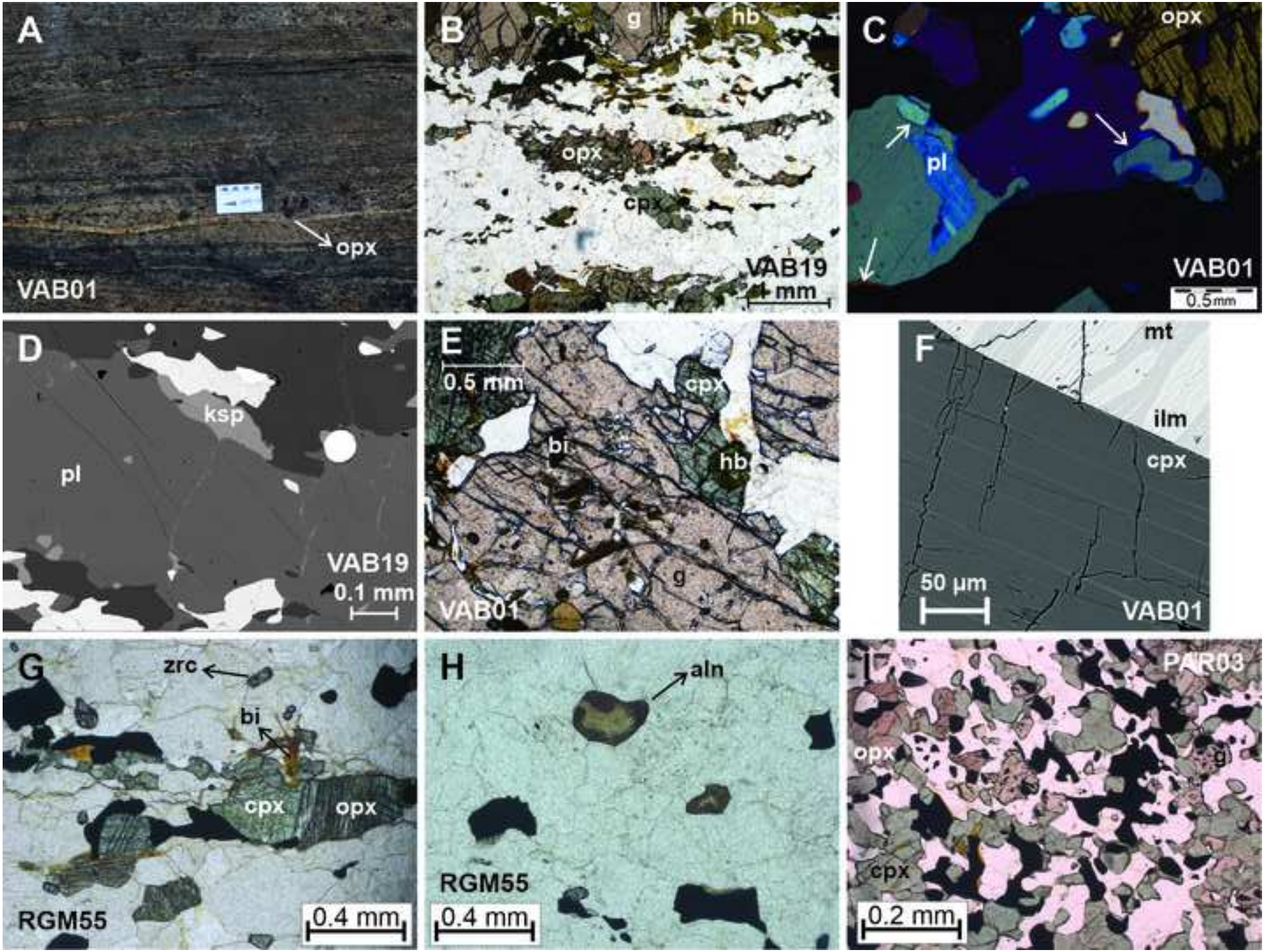

Figure 3

Click here to access/download;Figure;Fig 3.tif

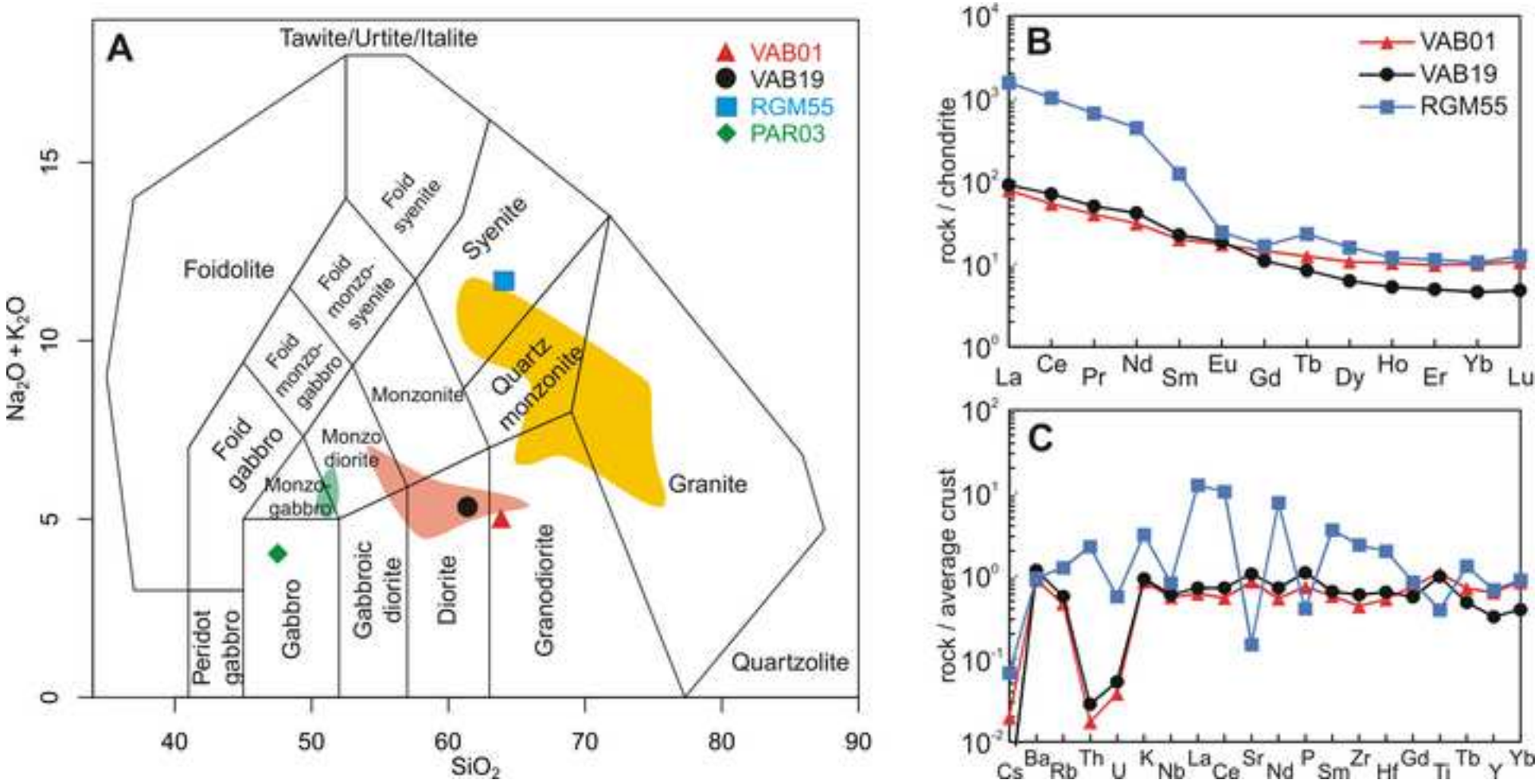

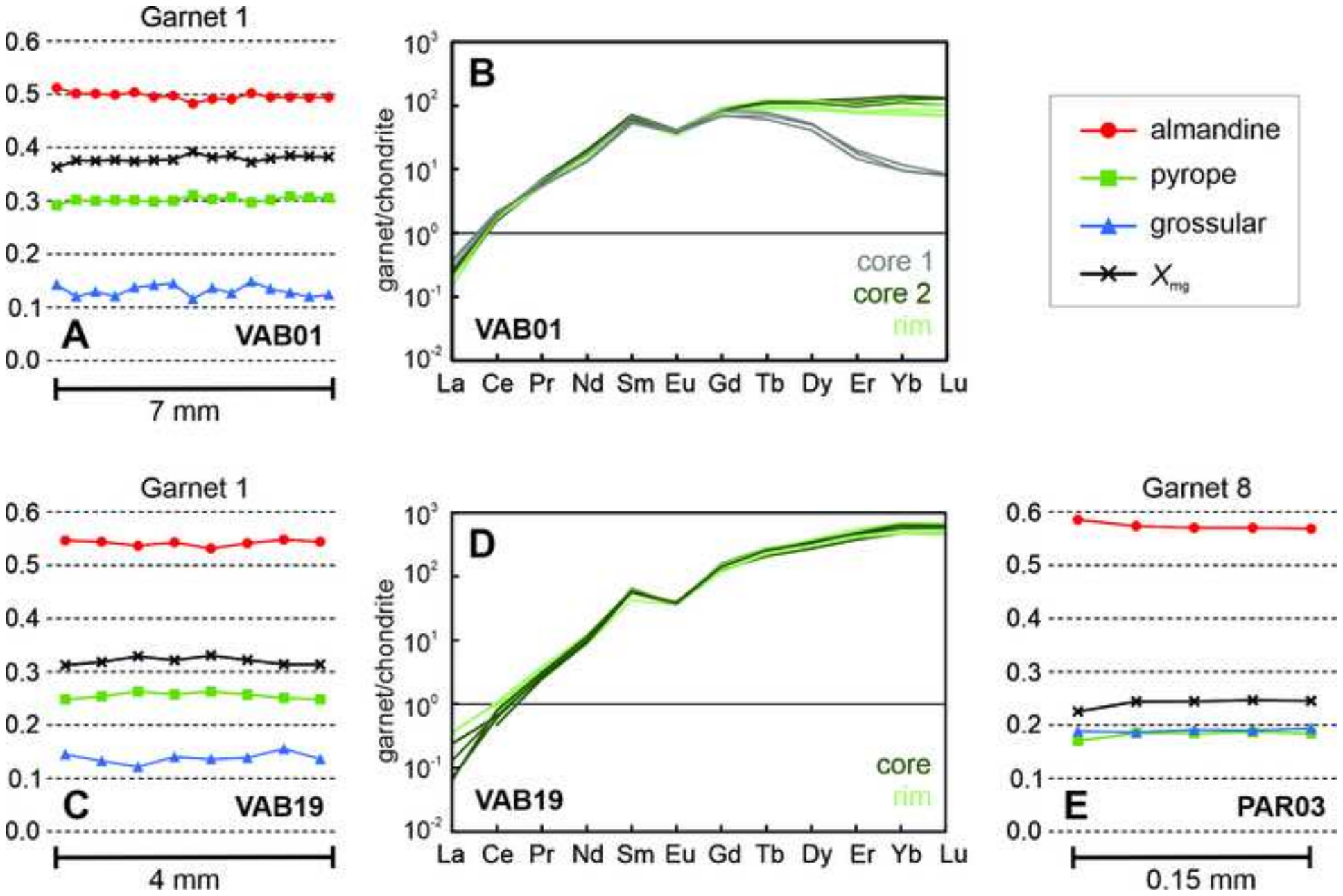

Figure 5

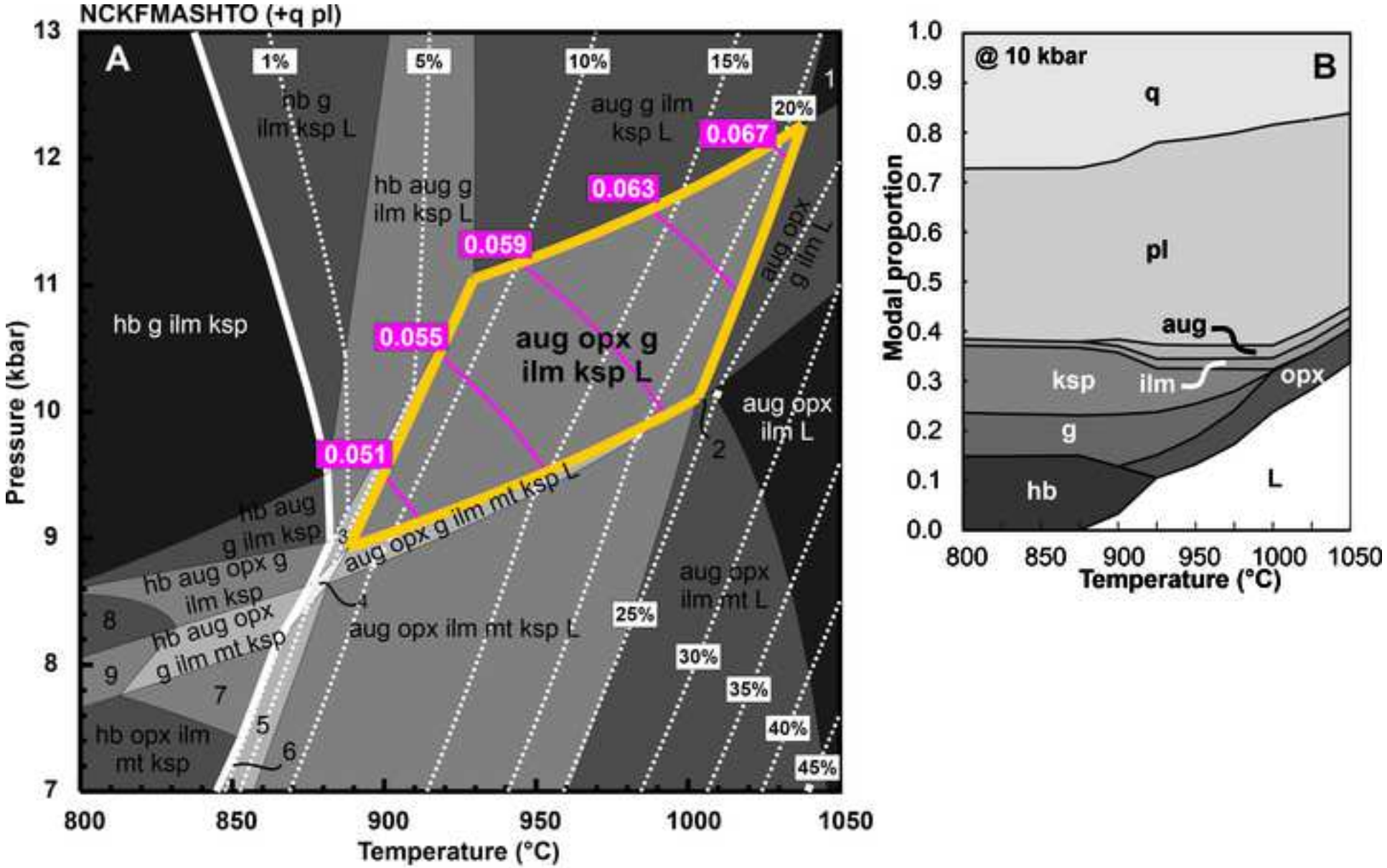

Figure 6

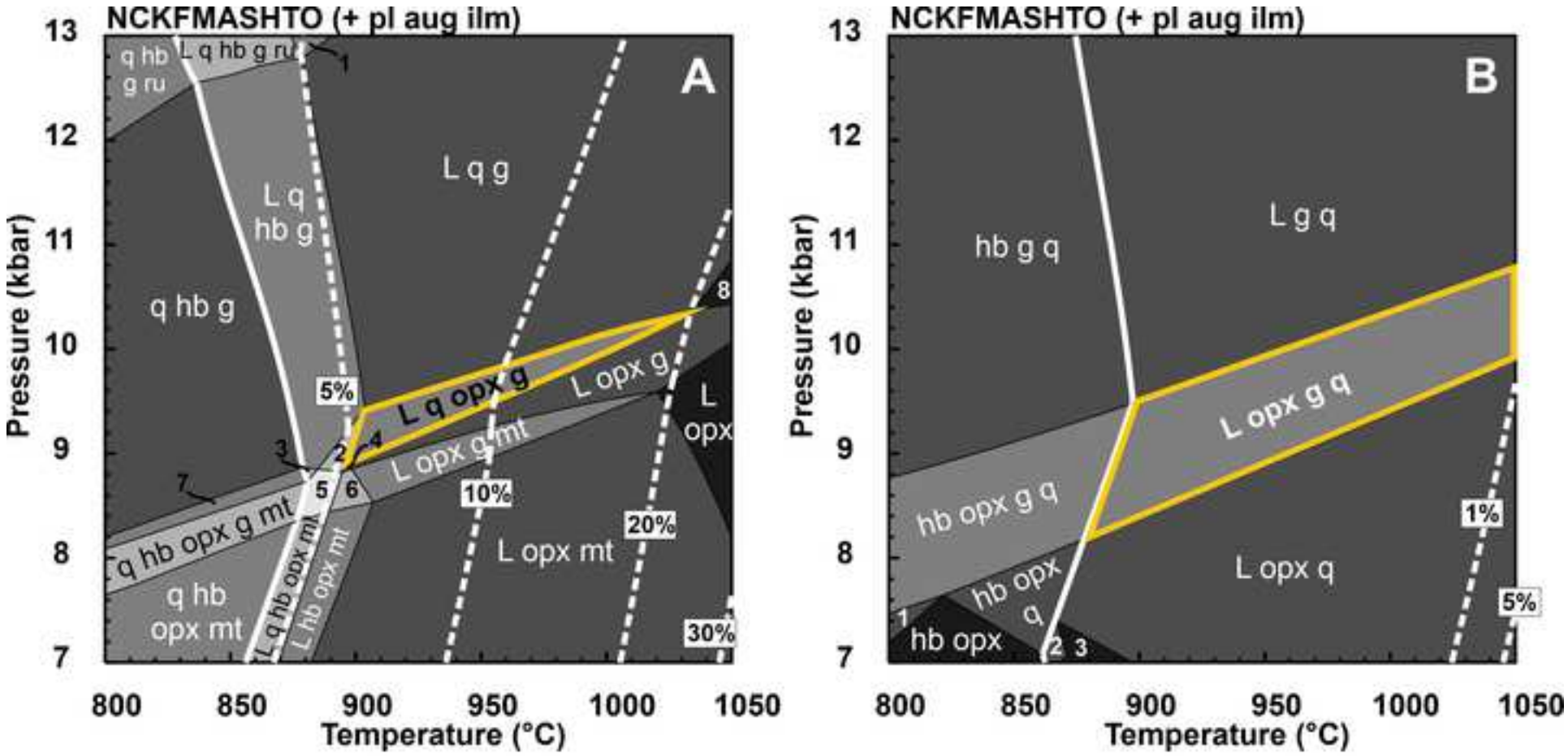

1 L q g ru
2 L q hb opx g
3 L q hb g mt
4 L hb opx g
5 L q hb opx g mt
6 L hb opx g mt
7 q hb g mt
8 L g

1 hb opx g
2 L hb opx
3 L opx

Figure 7

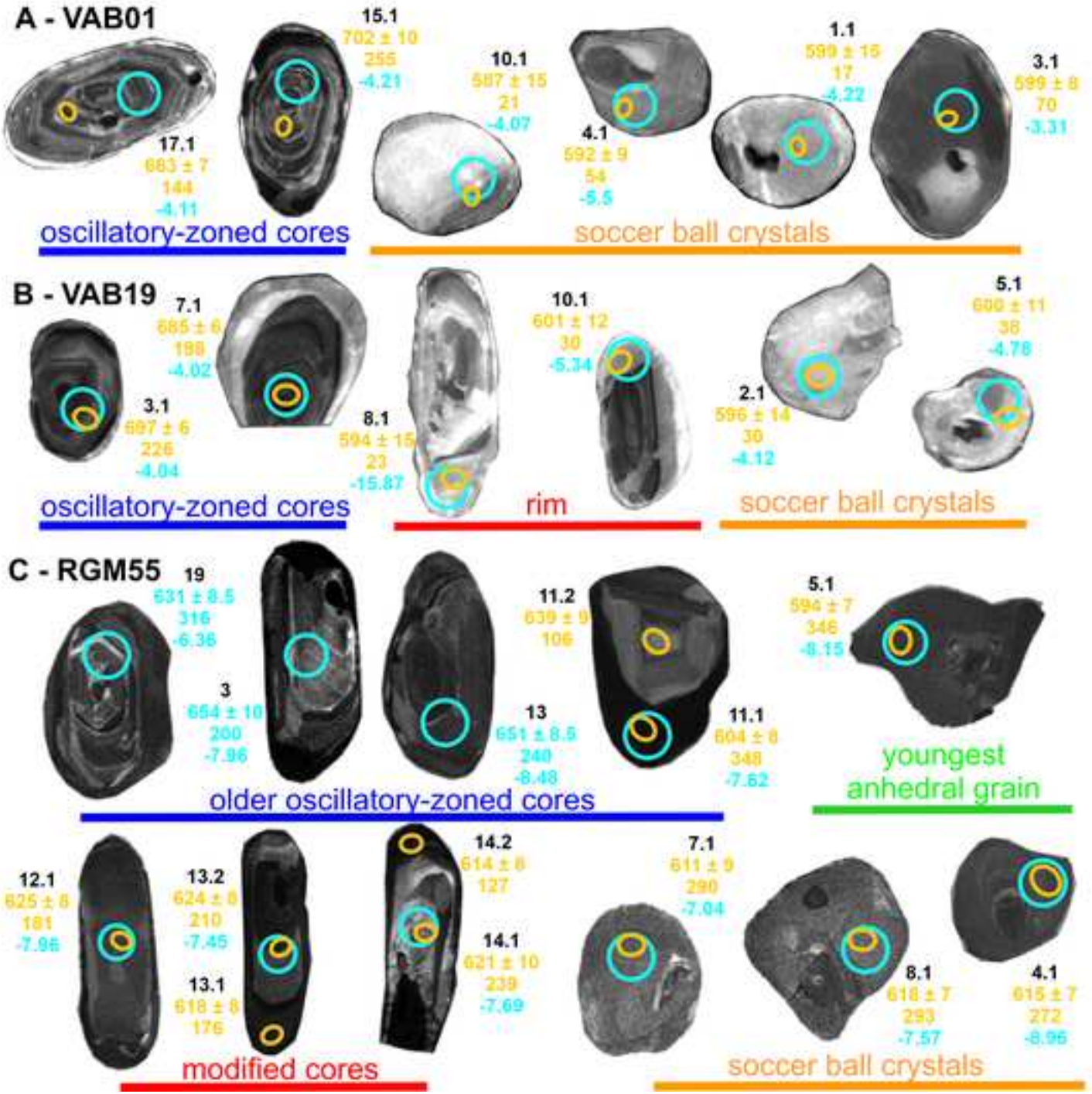

Figure 8

Click here to access/download;Figure;Fig 8.tif

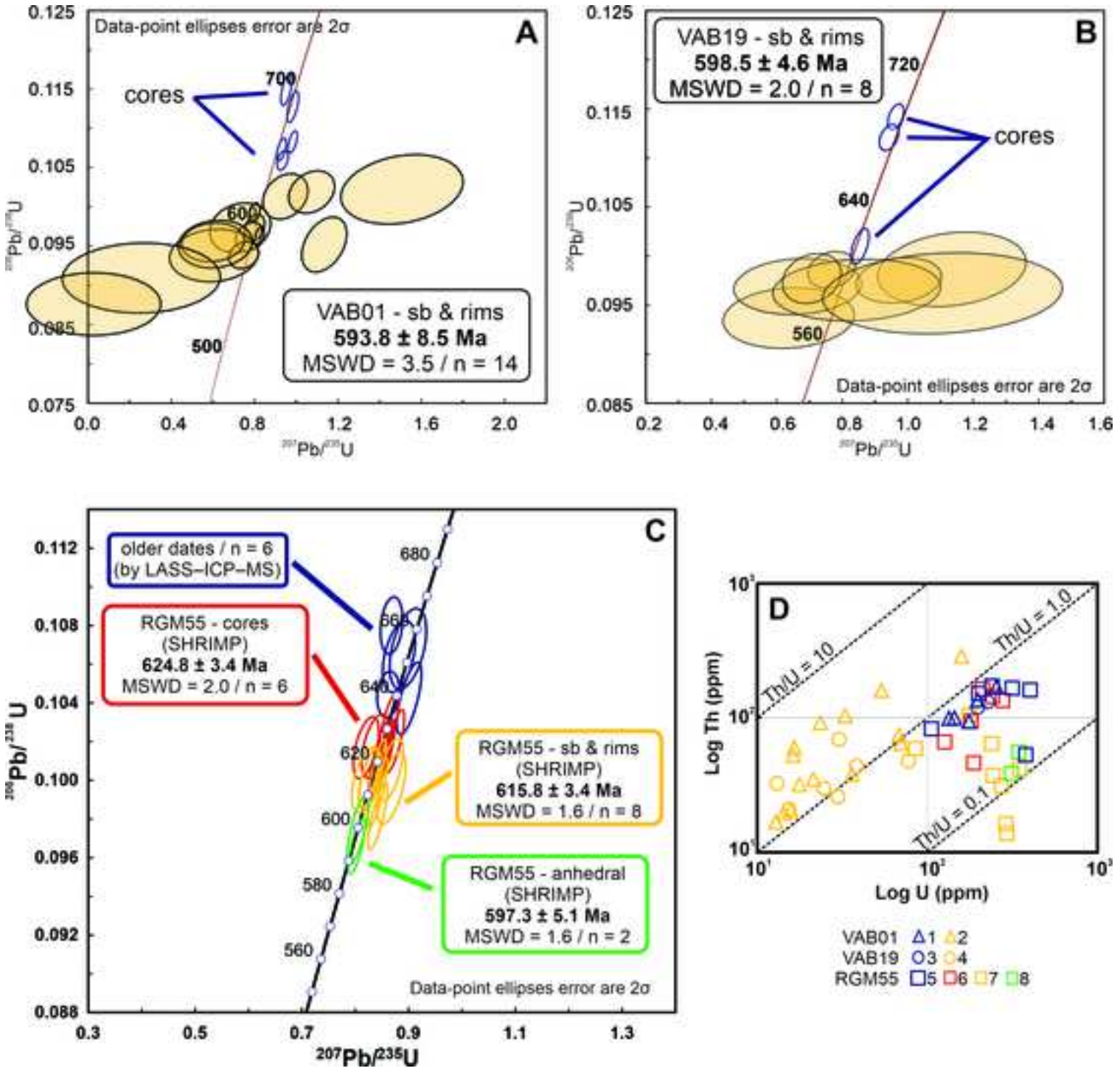

Figure 9

Click here to access/download;Figure;Fig 9.tif

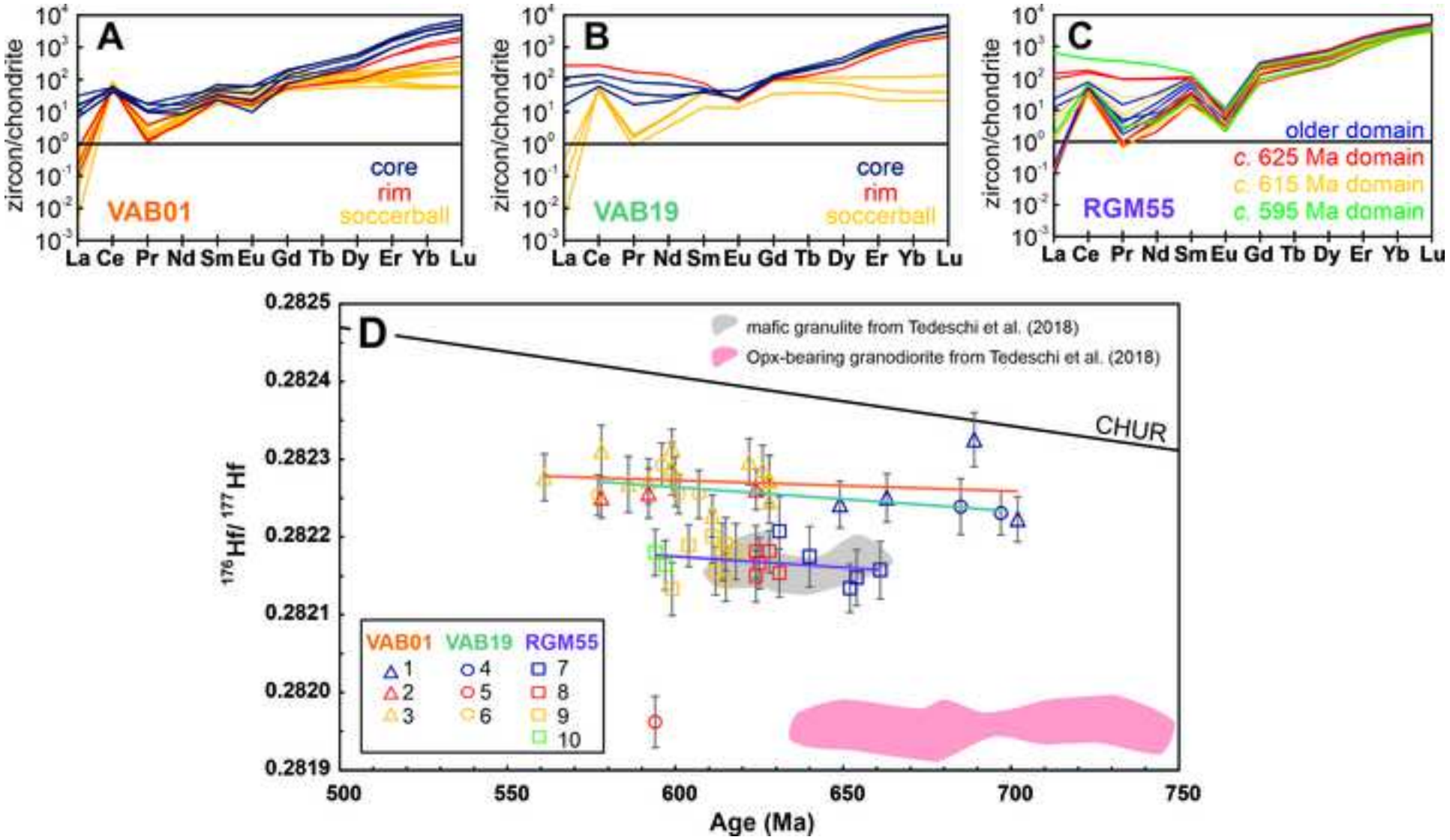

Figure 10

Click here to access/download;Figure;Fig 10.TIF

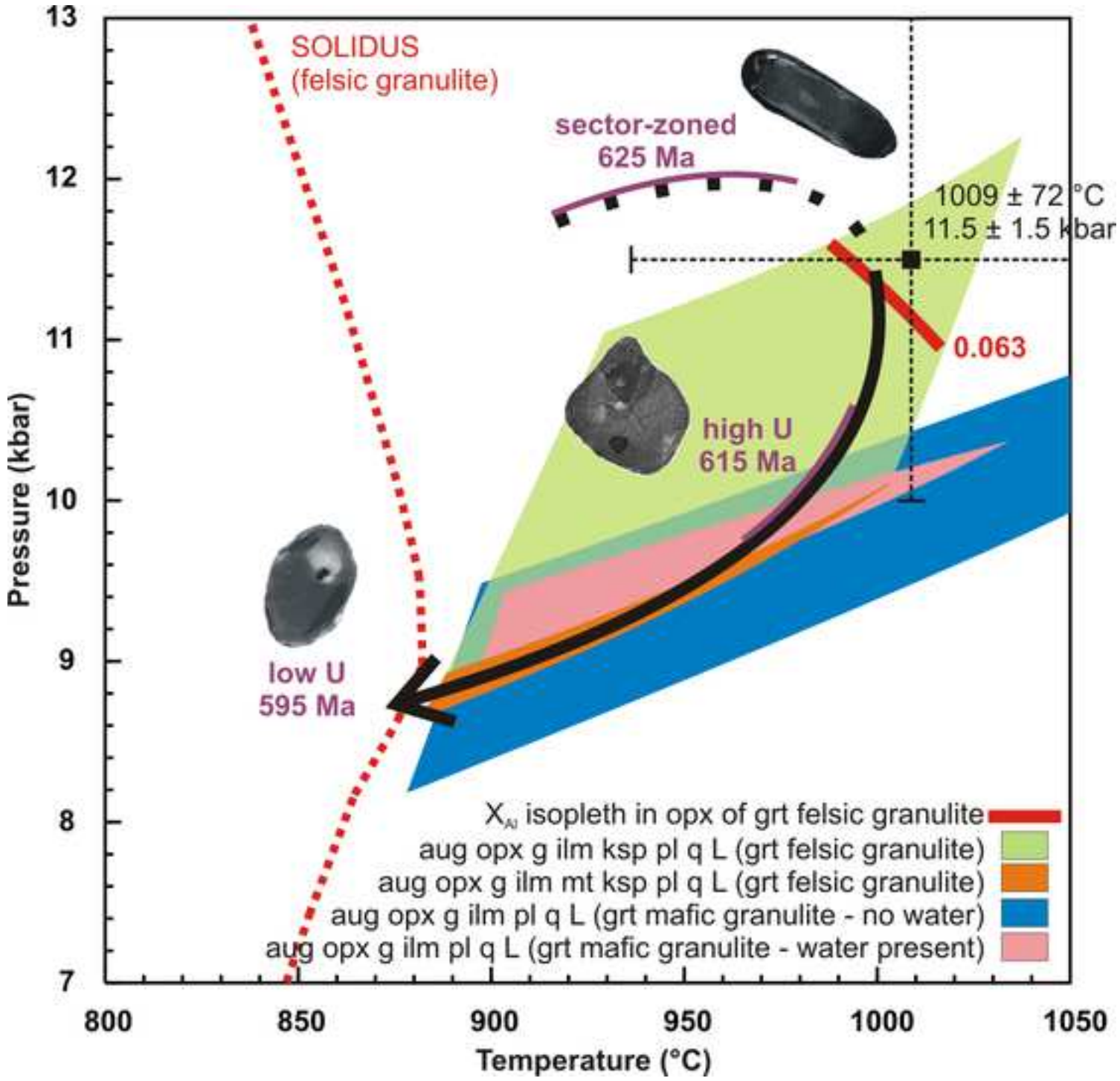

Figure 11

Click here to access/download;Figure;Fig 11.TIF

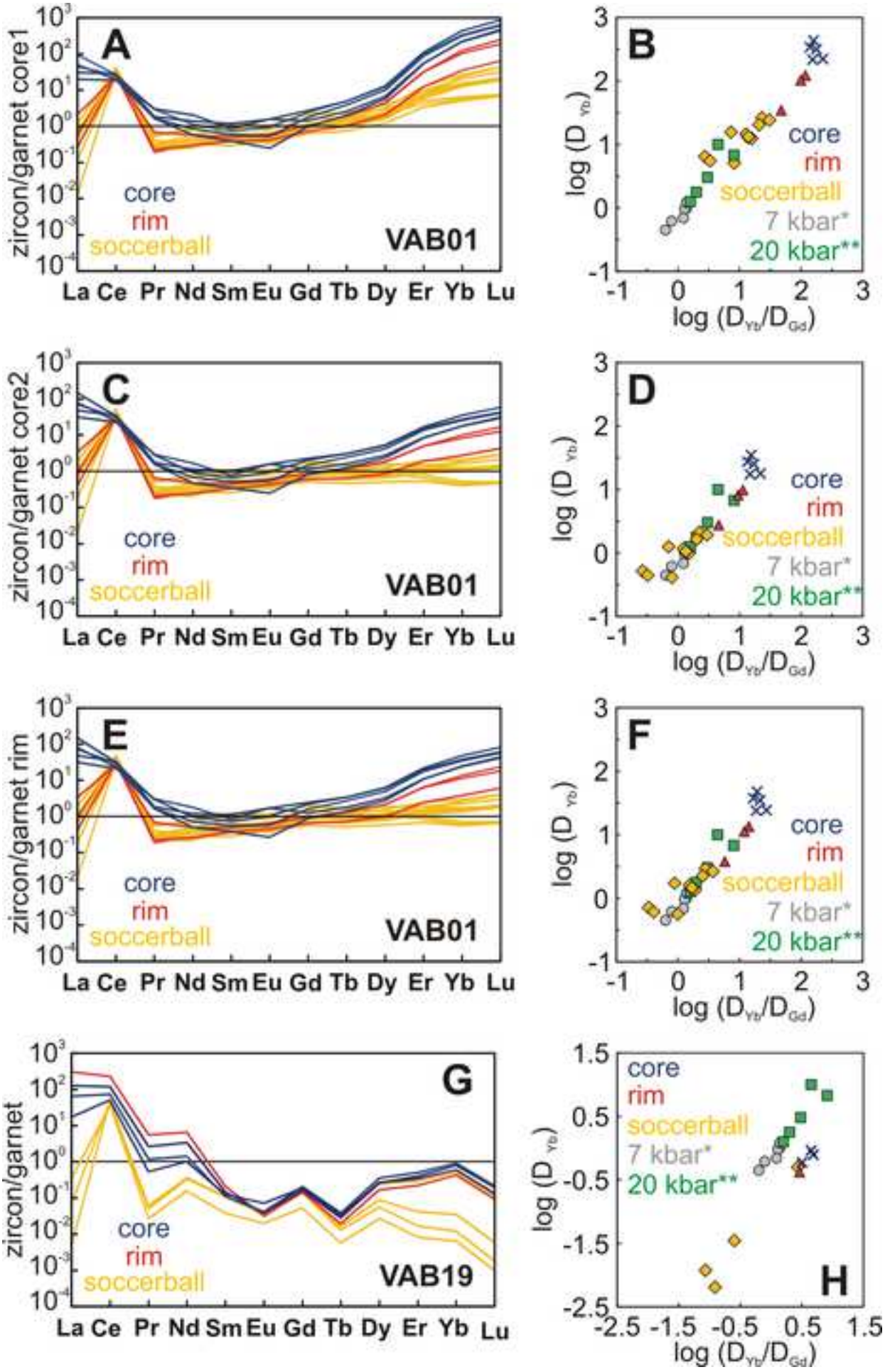

Figure 12

Click here to access/download;Figure;Fig 12.tif

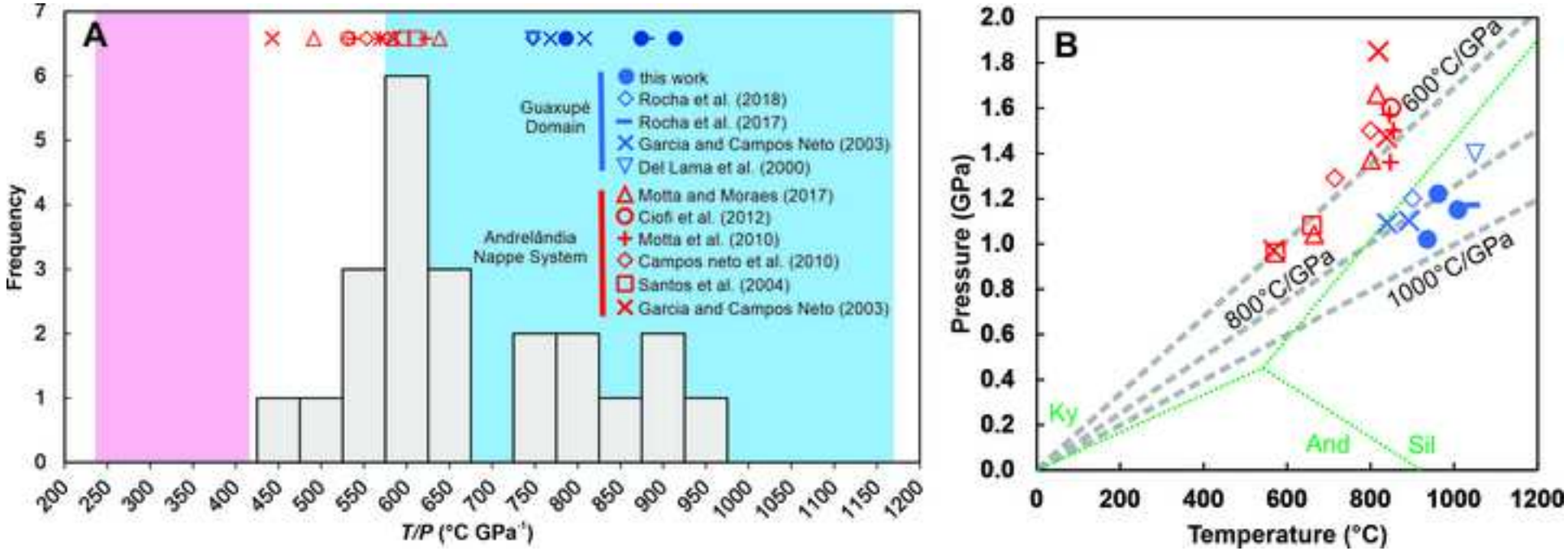

Table 1

Sample	Lithology	Figs.	H_2O	SiO_2	Al_2O_3	CaO	MgO	FeO	K_2O	Na_2O	TiO_2	O
VAB01	Grt felsic granulite	4, 5, 6, S1 and S2	1.00	68.34	9.67	5.63	3.88	5.37	1.43	3.11	0.57	1.00
PAR03	Grt mafic granulite	7A	1.00	48.38	7.74	11.28	7.91	14.78	0.1	3.05	2.28	3.48
		7B	0.01	48.84	7.81	11.39	7.98	14.91	0.1	3.08	2.3	3.58

Sample	Analysis used (see Table S1)	THERMOCALC *T* (°C)	*P* (kbar)	Pattison et al. (2003) *T* (°C)	*P* (kbar)	*T* (°C) at fixed *P* (11 kbar)
VAB01	cpx(reint)*-opx3.7-pl2.5**-grt1.8	1009 ± 144	11.5 ± 3	1020	14.4	936
VAB19	cpx2.2*-opx9c-pl4.2**-grt1.5	962 ± 148	12.2 ± 3	952	13.5	894
PAR03	cpx7.1*-opx1.3-pl3.3**-grt8.3	936 ± 186	10.2 ± 2.2	919	11	921

* clinopyroxene analysis are not used in the Pattinson et al. (2003) thermobarometer.
** at fixed pressures plagioclase is not used in the Pattinson et al. (2003) thermometer.